Universite du Quebec

INRS Energie Materiaux Telecommunications

Multiferroic Materials as Active Elements for Photovoltaic Devices

By

Joyprokash Chakrabartty

Memoire Presente

Pour l'obtention

du grade de Maitre es sciences (Energy and Materials)

(Jury d'evaluation)

President du jury	Monsieur Andreas Peter Ruediger
et examinateur interne	INRS Energie Materiaux Telecommunications
Examinateur externe	Monsieur Pablo Bianucci
	Concordia University, Canada
Directeur de recherche	Monsieur Federico Rosei
	INRS Energie Materiaux Telecommunications

Multiferroic Materials as Active Elements for Photovoltaic Devices

By

Joyprokash Chakrabartty

Dissertation

Submitted to INRS-EMT, University of Quebec,

in partial fulfillment of the requirements for the degree of

Master of Science in Energy and Materials

Research Supervisor: Federico Rosei, Professor and Director, University of Quebec, INRS-EMT, Canada

Advisory Committee:

Prof. Federico Rosei, INRS-EMT (supervisor)

Prof. Andreas Peter Ruediger, INRS-EMT (President of the Committee)

Prof. Pablo Bianucci, Concordia University (External Member)

Abstract

The discovery of bulk photovoltaic (BPV) effect in multiferroic (MF) materials has opened new perspectives in the field of photovoltaics (PV), because the photogenerated charge carriers are separated by an electric field which is not bound to a specific site, or interface. Instead, the mechanism of carrier separation in MFs relies on the electric field created by the spontaneous polarization present in the non-centrosymmetric material. Additionally, when the characteristic dimension of the material is decreased down to nano scale, for example in a multiferroic thin film, the polarization-induced electric field is even more intense. Thus, MF materials eliminate the need for n-p junctions that are usually employed in conventional semiconductor PV devices. However, the electrical power conversion efficiency (PCE) of BPV effect-based devices under sun light illumination is poor, and to date still not comparable with the conventional n-p junction based PV devices. The main reason for this is the low bulk photoconductivity of oxide based MFs, since the BPV originates in the ferroelectric properties, and ferroelectrics are insulating in nature. Therefore, the ultimate challenge in developing competitive devices using the BPV effect is to improve the conductivity by preserving the built-in spontaneous polarization of such type of material. Nonetheless, the energy band gap of MFs (~1.2-2.7 eV), an important parameter for photo carrier separation, is smaller than ferroelectric materials (~3-4 eV). Therefore, we dedicated our work to the development of novel MF materials or heterostructures that would result in PV devices with competitive PCE.

In first part of our work we developed a multi-stacking scheme, more specifically a heterostructure based on several $BiFeO_3/BiCrO_3$ (BFO/BCO) epitaxial bilayers grown by pulsed laser deposition (PLD) onto (100)-oriented LaAlO3 (LAO) substrates coated with conductive $CaRuO_3$ (CRO) buffer layers. When used as active layers in PV devices, these heterostructures showed a remarkable PCE of ~0.01% when illuminated with 1 sun (AM 1.5G). The fill factor (FF) was determined to be 31%, a prominent value for both ferroelectric- and MF-based devices. Our results demonstrate that photocurrent density and photovoltage can be tuned by varying the thickness and number of bilayers, opening new perspectives for the design of novel MF heterostructures with improved PV properties, tuned via engineered interfacial layers.

In the second part, we focused our efforts to the study of the BPV effect in thin films of Bi-Mn-O material system. The films were again grown by PLD on (111) oriented Niobium doped $SrTiO_3$ single crystal substrates. Detailed X-ray diffraction studies show that the films consist of two main phases, the perovskite $BiMnO_3$ (BMO) with a $(111)_m$ orientation, and Mn_3O_4 phase having the $(101)_t$ orientation. As revealed by Φ-scan measurements, both phases are epitaxially grown onto substrates. For PV tests we deposited transparent tin doped indium oxide (ITO) top electrodes, and we illuminated the devices using a sun simulator (AM 1.5G). Our findings show that the elemental Bi/Mn ratio in the films controls the magnitude of the photovoltage and photocurrent. Higher Bi/Mn ratio results in an increased PCE, and we obtained a maximum PCE of ~0.1% for the Bi/Mn ratio of 0.82. Film-electrode interfacial effect, modulated by ferroelectric polarization of the film has employed as a model to describe the observed PV phenomena.

Acknowledgement

I am truly fortunate to have spent more than two years at National Institute for Scientific Research (INRS-EMT), University of Quebec, Canada, that provided me the great opportunity to accomplish my graduate studies in a friendly environment. I would like to express my sincere gratitude to Professor Federico Rosei, my supervisor, for all generous supports he has given me throughout my M.Sc studies.

I would like to give thanks Dr, Riad Nechache, postdoctoral fellow, for spending his valuable time to get me involved in experiments and research very fast. Then I would like to take a chance to give thanks to Prof. Andreas Peter Ruediger for his scientific comments on a part of my works. I am indebted to all group members specially Mr. Shun Li and Mr. Daniel Obi, doctoral students, from whom I got unconditional supports. Special thanks also go to Dr. Catalin Harnagea for his comments on my dissertation. I am also grateful to all lab technicians, administrative staffs, and all professors of EMT-INRS for their direct and indirect supports.

Last, but not the least, I thank my parents who gave me true love and unwavering support during these two years. Therefore, I am honored to dedicate my dissertation to my parents.

Table of Contents

Table of Figures

List of Tables

Introduction

The discovery of optoelectronic properties in ferroelectric perovskite thin films has paved the way for the exploration of new approaches for energy conversion including photovoltaic (PV) applications. Without the need for n-p junction, ferroelectric polarization of such thin films induces a strong internal electric field which can be used to separate photo generated charge carriers, thus producing a photovoltage. This effect was named bulk photovoltaic effect (BPV). In addition to the BPV effect, it has been shown that there is a potential drop across certain types of domain walls in the ferroelectric material, which, for a particular geometry of the domain structure, results in a total photovoltage (V_{oc}) that exceeds by far the bandgap of the material. [1] The most widely investigated multiferroic materials for those applications are $BiFeO_3$ (BFO) and Bi_2FeCrO_6 (BFCO). BPV properties have been discovered in numerous ferroelectric materials such as $LiNbO_3$,[2,3] $BaTiO_3$[4] and $Pb(Zr,Ti)O_3$.[5] To date, La-doped epitaxial $Pb(Zr,Ti)O_3$ thin films exhibit the highest power conversion efficiency (~ 0.005%) under sun light [6], 10% external quantum efficiency of BFO [7] and 6% of BFCO [8] under red light illumination. In Bi-containing perovskite materials, spontaneous polarization is created by the displacement of Bi ions, occurring due to the effect of $6s^2$ lone pair electron.

Due to the coexistence of ferroelectricity and magnetic order (i.e. transition metal ions with unpaired d electrons), epitaxial multiferroic films [9,10] are interesting materials for PV applications since they typically have strong unidirectional ferroelectric polarization and smaller band gaps (typically ~1.7-2.7eV) compared to conventional ferroelectric materials (~3.5 eV). $BiMnO_3$ has one of the lowest band gaps, it is reported as the "hydrogen atom" of multiferroic materials in Ref. [11], and thus it is another promising candidate for PV applications.

However, the external power conversion efficiency of those materials is still poor and also is under debate. Indeed, the observed photocurrents are insignificant, of the order of nA/cm^2, mainly due to the wide bandgap of ferroelectric (typically 3-4 eV) and their high electrical resistivity. As a result, devices based on ferroelectric films as active layers are not considered promising for PV applications in practice. However, there are two recent reports that changed these believe: the first, by. Yang et al. [1] demonstrating the PV effect within domain walls and

the generation of a very high open circuit photo voltages (~15V). A second report, by M. Alexe and Hesse [12] demonstrated a drastically enhanced PV effect (up to 30 V photovoltage) from the single crystal BFO when the top electrode is very sharp. While these two reports apparently contradict each other, one promoting the domain wall PV concept, the other the BPV effect, we believe that they are different facets of a more intricate effect that occurs in these complex materials.

The main objectives of this thesis are to investigate the photovoltaic properties in complex oxide functional materials. It is expected that when the dimension of these types of materials goes down to nanoscale (the thickness of thin films in our case), they show interesting properties compared with their bulk counterpart. The main challenges here are to improve the external power conversion efficiency because multiferroic materials are insulating in nature. Like many others, we tried in this work to improve the efficiency by engineering these types of materials. To do so, we used epitaxial $BiFeO_3$, and $BiCrO_3$ thin films, periodically multistacked, deposited on a $CaRuO_3$ coated $LaAlO_3$ perovskite substrate by pulse laser deposition (PLD). Our observation shows remarkable power conversion efficiency and that spontaneous ferroelectric polarization plays a key role in the PV effect. Another part of our work was dedicated to the investigation, of the photovoltaic efficiency of the Bi-Mn-O thin film system deposited on Nb doped $SrTiO_3$ perovskite substrate. Ferroelectric polarization modulated film/electrodes interfacial effect has been employed here to explain the observed photovoltaic effect.

References

[1] S. Y. Yang, J. Seidel, S. J .Byrnes, P. Shafer, C.-H. Yang, M . D .Rossell, J. F. Scott, J. W. Ager, L.W. Martin, P. Yu, Y.-H. Chu, and R. Ramesh, Nature Nanotech. **5**, 143 (2010)

[2] A. M. Glass, D. von der Linde, and T. J. Negran, Appl. Phys. Lett. 25, 233 (1974)

[3] A. M. Glass, D. Von der Linde, D. H. Auston, and T. J. Negran, J. Electron. Matter. 4, 915 (1975)

[4] V. M. Fridkin and B. N. Popov, Sov. Phys. Usp. 21, 981 (1978)

[5] P. S. Brody and F. Crowne, J. Electron. Matter. 4, 955 (1975)

[6] M. Qin, K. Yao, and Y. C. Liang. Appl. Phys. Lett. 93, 122904 (2008)

[7] S. Y. Yang, L. W. Martin,S. J. Byrnes,T. E. Conry,S. R. Basu,D. Paran, L. Reichertz, J. Ihlefeld, C. Adamo,A. Melville,Y.-H. Chu, C.-H. Yang, J. L. Musfeldt,D. G. Schlom, J. W. Ager and R. Ramesh, Appl. Phys. Lett. 95, 062909 (2009).

[8] R. Nechache, C. Harnagea, S. Licoccia, E. Traversa, A. Ruediger, A. Pignolet, and F. Rosei Appl. Phys. Lett. 98, 202902 (2011).

[9] J. Wang et al. Science 299, 1719-1722 (2003)

[10] R. Nechache, C. Harnagea, A. Pignolet, F. Normandin, T. Veres, L. -P. Carignan, and D. Ménard, Appl. Phys. Lett. 89, 102902 (2006)

[11] N. A. Hill and K. M. Rabe, Phys. Rev. B 59, 8759 (1999).

[12] M. Alexe, Nano Letters **12**, 2193-2198 (2012).

Chapter 1 Properties of Multiferroic Material in Photovoltaics

1.1 Introduction

Nanotechnology deals with small structures or small sized materials. Typical dimensions of interest in nanotechnology are from several subnanometer to several hundred nanometer. A nanometer is one billionth of a meter (1nm $=10^{-9}$ m). For more visualization, one nanometer is approximately the length equivalent to ten hydrogen or five silicon atoms aligned in a row. The idea of nanotechnology first comes from an important talk "There's Plenty of Room at the Bottom: an Invitation to Enter into a New Field of Physics" given by Nobel Laureate Richard Feynman in 1959 at the California Institute of Technology (CalTech) [1]. Since then scientists have been investigating the impact of nanotechnology that can play a vital role in every aspect of society. The term "nanotechnology" was first initiated by Professor Norio Taniguchi of Tokyo Science University in 1974. According to him, "Nano-technology' mainly consists of the processing of separation, consolidation, and deformation of materials by one atom or by one molecule". [2] Later on, the discovery of scanning tunneling microscope (STM) in 1981 opened up an era to see atomic clusters in a material, as a consequence of that, Eigler and E. Schweizer in 1990 from IBM-Almaden Research Centre, California, showed up their ability to arrange individual xenon atoms forming the IBM logo on a single crystal nickel surface using STM tip at low temperatures (4K). [3]

The Physical properties of a material at micrometer scale are mostly the same as that of bulk form, however, decreasing its size in the nanometer range, it exhibits distinctively different properties than that of bulk form. Dramatically increased surface area, surface roughness and surface area to volume ratios due to the decreasing material size down to the nanoscale, leads to higher physicochemical properties such as mechanical, electrical, optical, catalytic, and magnetic properties [4]. Therefore, nanotechnology is not only a simple continuation of miniaturization from micrometer down to nanometer scale but also the control of material properties by assembling nanostructures atom by atom or molecule by molecule. Since the field of

nanotechnology is diverse, starting from the study of microstructures of materials to nanostructures to enabling bottom up approach in materials synthesis and fabrication even in terms of biological application, none of them covers the full spectrum of the definition of nanotechnology. In general, nanotechnology is a technology of design, fabrication, and applications with diverse understanding of physical properties and phenomena of nanomaterials and nanostructures. Nonetheless, nanoscience refers to the fundamental study on the relationships between physical properties and phenomena and material dimensions in the nanometer scale. [5] The most widely accepted definition of nanotechnology in the United States as follows: "concerned with materials and systems whose structures and components exhibit novel and significantly improved physical, chemical and biological properties, phenomena and processes due to their nanoscale size". [6] Thin films, nanowire, quantum dots are examples of the most widely investigated nanostructured materials now a days.

1.2 Magnetism and Ferroelectricity

The magnetism in a material lies in the orbital and spin motions of electrons and the way of interaction of electrons with one another. Whether a material is magnetic or not, depends on the response of that material under applying magnetic fields. Most materials are magnetic in a sense but some of them show higher magnetism than others. The main reason of showing this difference is that there is no collective interaction of atomic magnetic moments in some materials, whereas in other materials there is a very strong interaction between atomic moments. The magnetic behavior of materials is classified as follows: i) diamagnetism ii) paramagnetism iii) ferromagnetism iv) ferrimagnetism and v) antiferromagnetism. The distinction between the different types of magnetism lies on the collective magnetic interactions and ordering of the magnetic entities present in the material. **Figure 1.1** shows different types of magnetic ordering based on such type of interaction and ordering.

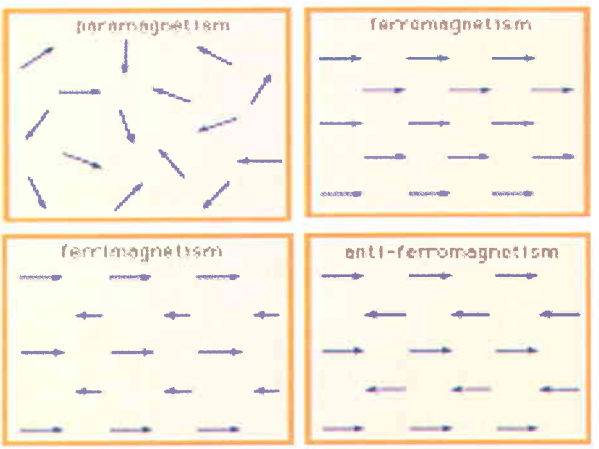

Figure 1.1 Schematics of different types of magnetic ordering [7]

A crystal is said to be ferroelectric when it possesses at least two equilibrium orientations of the spontaneous polarization vector in the absence of an external electric field, and the spontaneous polarization can be switched between those orientations by an electric field [8].The distinct characteristic of a ferroelectric is the spontaneous polarization (P), which is a reversible polar vector. It develops as a result of a symmetry reducing phase transformation that displaces positive and negative charges along a restricted family of crystallographic directions, resulting in a permanent electric dipole moment [9]. To be ferroelectric, this dipole moment must have two or more crystallographic equivalent directions. Ferroelectricity was first discovered by Valasek in 1921 in Rochelle salt.

1.3 Primary Ferroics

A ferroic is a material that exhibits spontaneous and switchable internal alignment by an external stimulus. The primary, well established types of ferroic materials are ferroelectric, ferromagnetic and ferroelastic shows spontaneous electric polarization, spontaneous magnetisation and spontaneous strain. The alignment of electric dipole moment in ferroelectrics, alignment of electron spins in ferromagnetics and strain alignment in ferroelastics can be switched by their conjugate quantities, i.e. the electric, magnetic and strain field, respectively [10]. In general, ferroic materials exhibit a hysteretic behavior when the external driving force is cycled, as shown in **Figure 1.2**.

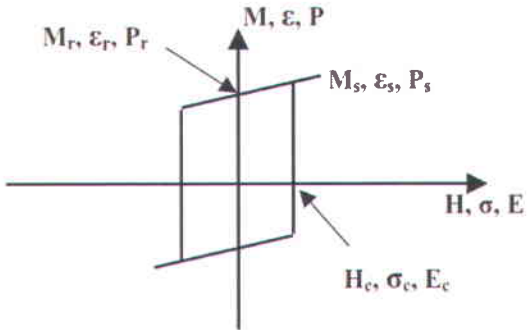

Figure 1.2 Schematic of a hysteresis loop showing coercive field, remnant and saturation strain, polarization and magnetization **[11].**

1.4 Definition of Multiferroic (MF) Material

Any material that exhibits more than one primary ferroic ordering in the same phase [12] is called multiferroic. A particularly important class of multiferroics is that which comprises ferro-electricity and one type of magnetic order in the same phase. It covers not only ferroic ordering but also anti-ferroic ordering. For an example, $BiFeO_3$ most widely investigated multiferroic compound, exhibits both ferroelectricity and anti-ferromagnetism at room temperature.

Mutiferroics can be classified into two groups: materials with independently originating ferroelectricity and magnetism, and materials in which magnetism causes ferroelectricity. The second group brings one of the most appealing aspects of multiferroic material and is referred to as 'magnetoelectric (ME) multiferroics". The interdependence of the relevant quantities in such a material is shown in **Figure 1.3** that extends its application into spintronic.

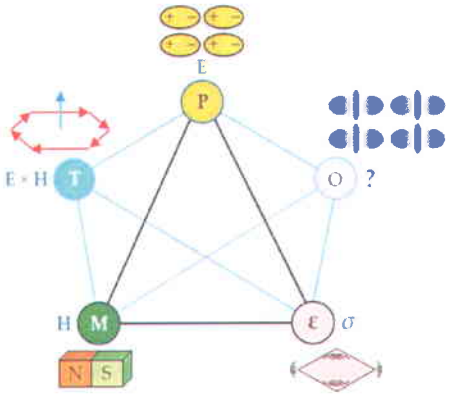

Figure 1.3 Schematics of coupling interactions in multiferroics.'T' represents torroidal moments and 'O' represents other possibilities of coupling such as spontaneous switchable orbital orderings, vortices, and chiralities **[10].**

From the crystallographic structural point of view, multiferroic materials are divided into four classes: perovskite oxides e.g. $BiFeO_3$, $TbMnO_3$; hexagonal oxides e.g. $RMnO_3$ where R= Ho, Er, Tm, Yb, Lu, as well as Y and Sc; boracites e.g. $M_3B_7O_{13}X$ where M is a bivalent metal ion (M = Cr, Mn, Fe, Co, Cu, Ni) and X=Cl, Br, I; and $BaMF_4$ compounds where M= Mg, Mn, Fe, Co, Ni, Zn [13]. In our work, however, we focus on the perovskite structure, more specifically on the complex oxide perovskites because of its good ferroelectricity, large dielectric constants, ferromagnetism, and antiferromagnetism [14]. Most of the perovskites fall into this complex oxide group because it comprises two or more transition metal cations (typically 3d) with oxygen. In addition, oxides are abundant compounds on earth. The general chemical formula of the perovskite structure used in this work is ABX_3, or $A_2BB'X_6$ (for the double perovskite) where 'A' denotes nonmagnetic cation and 'B' denotes magnetic cation. **Figure 1.4** shows the typical perovskite unit cell of bismuth ferrite, $BiFeO_3$ (BFO). The rhombohedrally distorted perovskite BFO exhibits a prominent spontaneous polarization (~100 $\mu C/cm^2$ at room temperature) [15, 16] below the ferroelectric transition temperature (T_C = 1,103 K) giving antiferromagnetism below the antiferromagnetism Neel temperature (T_N=643K).

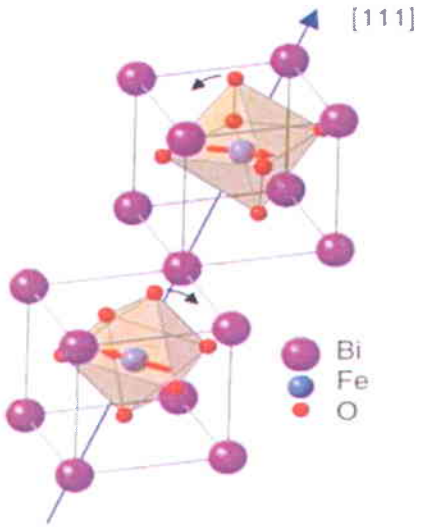

Figure 1.4 Schematics of typical structure of the $BiFeO_3$ compound [17]

In conventional ferroelectric materials, ferroelectricity originates from the non centrosymmetric nonmagnetic cation that shifts away from the center of the surrounding anions. The noncentro-symmetricity between positive and negative charges gives rise to the electric dipole moment. In contrast, in a magnetic material, the magnetic cation (having a partially filed d orbital) tends to sit exactly at the center of the surrounding anions, i.e the centrosymmtric position is favored, resulting in no dipole moment. Since both ferroelectricity and magnetism do coexist in the multiferroic material, it means there is a competition between the formation of energy-lowering covalent bond and the energy-raising electronic coulomb repulsion [8]. The compromise between them makes off-centering of the A site cation, Bi^{3+} in the case of BFO, to result in the apparition of a dipole moment, thus ferroelectric behavior. In other words, ferroelectricity can also generate from the structural instability which is compatible with the coexistence of magnetism [18, 19, 20].

1.5 Photovoltaics with Mutiferroic materials

In conventional n-p junction based PV devices, the photo generated charge carriers are driven by the electric field [21] created at depletion region. This means that the open circuit voltage (V_{oc}) in this case is limited by the band gap of the material, normally less than the band gap ($eV_{oc} < E_g$). In contrast, in the case of the photovoltaic effect in ferroelectrics, the photo

generated electrons and holes are further separated by the internal electric field present in ferroelectric materials, which originates from the inbuilt spontaneous polarization [22]. The basic difference between these two types of PV devices lies in the magnitude and the range of their carrier driving force i. e. the electric field. Polarization-dependent electric field (i. e. depolarization field, E_{DP}) in the ferroelectric material is at least an order of magnitude higher than in conventional n-p junction based devices. In addition, the depolarization field is not confined in a small zone as is the case of the p-n interface. Similar to the n-p junction, lower band gap MFs possess ferroelectric behavior that develops electric field in the whole volume of the material, a critical issue for photo charge carrier separation in PV devices. The mechanism of photovoltaic effect in MFs can be explained in similar fashion of p-n junction, shown in **Figure 1.5**. Here in the case of BFO thin film with a particular domain wall, the changes of abrupt polarization are occurred at the domain wall. This imbalance of charges [23] creates an electrostatic potential drop (typically between 0.02-0.2 eV) across the domain wall which is responsible for band bending in this region [24]. Note that the domain wall is much thinner (2 nm) than the depletion layer of a n-p junction, therefore, charge separation is much more effective and faster.

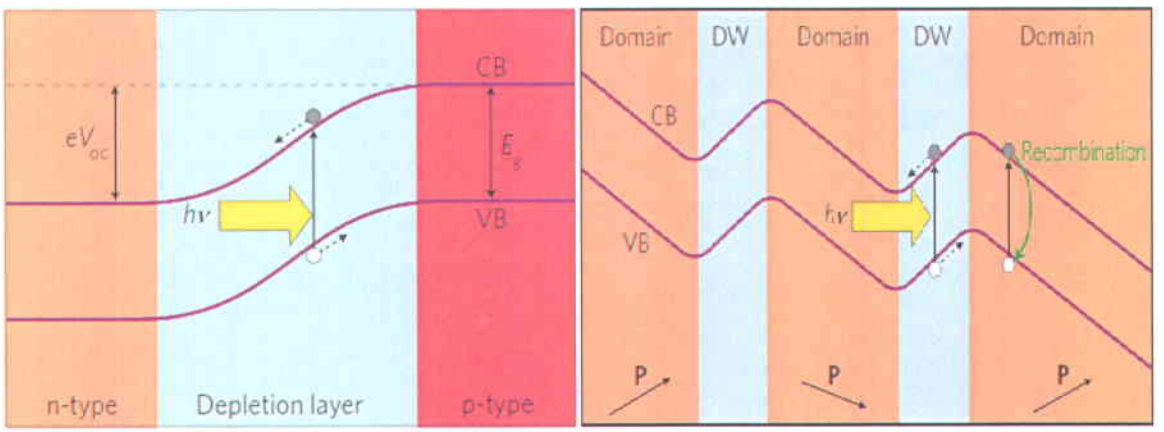

Figure 1.5 Schematics of the band diagram of conventional n-p junction (a) and band bending of alternative multiferroic photovoltaics (b). Adapted from reference-[24]

For thin film solar cells based on MFs, electrodes are also required to contact with the films that creates Schottky contact at film-electrode interface. Therefore, the photo charge carrier

driven total internal electric field is the combination of two components: (i) the depolarization field (E_{dp}) originating from the polarization alignment in the bulk of the film, and (ii) the net interface electrical field (E_i) resulting from the electrode-film interface. As illustrated in **Figure 1.6**, the depolarization field (E_{dp}) originates from spontaneous polarization and opposite to the direction of polarization, and the interface electric field (E_i) is polarization independent, and it originates from the Schottky contacts of the electrode-film interface.

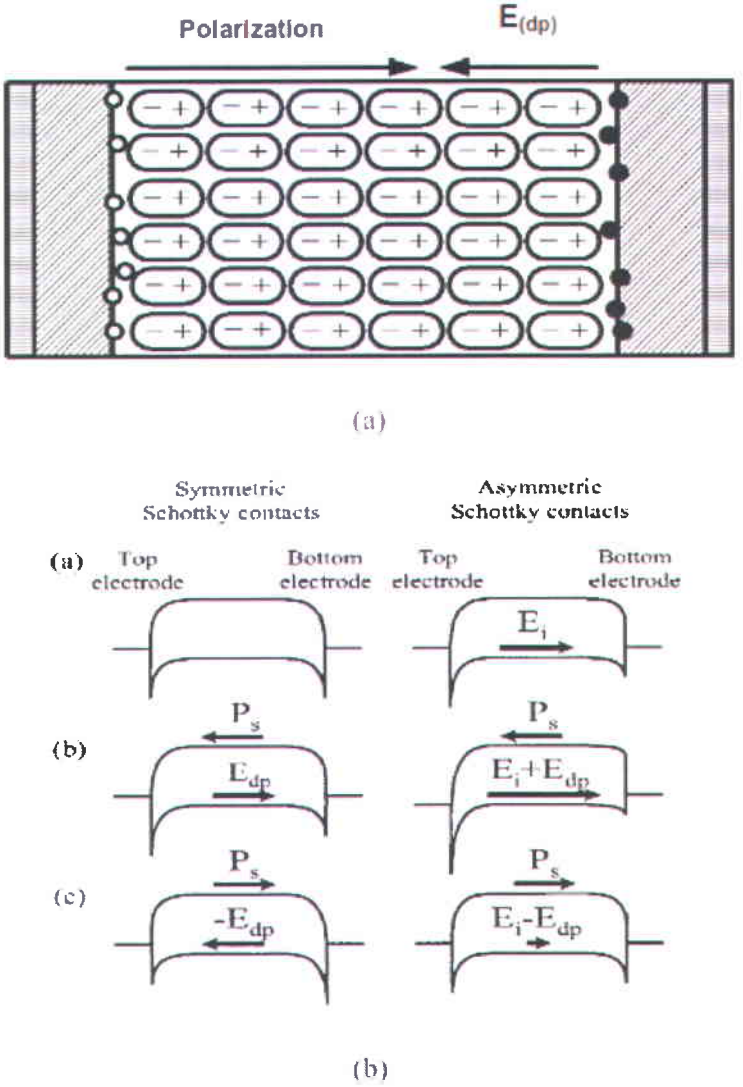

Figure 1.6 (a) The interfacial effect on the photo voltage in a ferroelectric material showing depolarized field (E_{dp}) [25] (b) Diagram of metal-film-metal having symmetric and asymmetric Schottky contacts indicating the interface electric field E_i [26]

However, power conversion efficiency of devices based on MFs is still poor due to the intrinsically low bulk conductivity, compared with that of a commercially available silicon based solar cell. This is explained as follows: for ferroelectricity to exist in a multiferroic material it must be insulator in nature, otherwise the mobile charges will screen out the electric polarization [27]. In fact, any efforts to rise up conductivity of ferroelectrics result in a lower spontaneous

polarization, and as a consequence, lower internal electric field. Since the latter is directly related with the separation of photo generated charge carriers, this results in lower power conversion efficiency. However, efficient synthesis of nano structure and material engineering could be an effective way of improving PV efficiency.

1.6 Structure of the thesis

Chapter 2 describes shortly the main experimental methods used throughout this works. Starting with the pulsed laser deposition technique (PLD), a prominent tool for complex oxide film growth, the effect of several key parameters on the quality of thin films is discussed. Then the chapter covers the different types of thin film characterization methods that have been used to analyze the result in this thesis. For example, X-ray diffraction (XRD) and Transmission electron microscopy (TEM) was used to analyze structure and morphology of as-deposited thin film. Atomic force microscopy (AFM) and Scanning electron microscopy (SEM) was used to visualize the surface topography and Piezoresponse force microscopy (PFM) proved the presence of ferroelectricity in thin film. Optical absorption and band gap were measured by spectroscopy ellipsometry. Finally, the experiments using a solar simulator are explained in short as they give the value of the photocurrent and the photovoltage, which are the basis for calculating the power conversion efficiency. Chapter 3 presents the experimental results of PV efficiency obtained on $BiFeO_3/BiCrO_3$ bilayer thin film deposited on $LaAlO_3$ substrates. The key finding is the dependence of photo current and photo voltage on number of bilayer incorporated in the structure. Thickness dependent absorption depth (Beer-Lambert Law) had been employed to explain the nature of observed photovoltage and photocurrent because of closer band gap of BFO and BCO layer. In Chapter 4, we report the photovoltaic effect in BMO thin films, a result that has never been reported before. We present a comparative study of the photovoltaic efficiency of three Bi-Mn-O thin films with different compositional ratios Bi:Mn, deposited on (111) oriented Nb doped STO perovskite substrates. Higher Bi/Mn ratio exhibits higher PCE. The observed PV phenomena are explained by the combined effect of ferroelectric polarization and film/electrodes interfacial. Chapter 5 concludes the thesis with a summary of our findings and future perspectives.

1.7 References

[1] Richard P. Feynman, Caltech Engineering and Science, Volume 23:5, pp 22-36, February 1960

[2] N. Taniguchi, Proc. of International Conference on Precision Engineering (ICPE), Tokyo, Japan, pp. 18—23, 1974

[3] D. M. Eigler and E. K. Schweizer, "Positioning single atoms with a scanning tunnelling microscope" Nature 344, 524 (1990)

[4] B. D. Fahlman, Materials Chemistry, Springer, Dordrecht, Netherlands, 2007

[5] Guozhong Cao (University of Washington, USA) and Ying Wang (Louisiana State University, USA), Nanostructures and Nanomaterials - Synthesis, Properties and Applications (2nd Edition) @ World Scientific Publishing Co. Pte. Ltd.

[6] National Nanotechnology Initiative 2000 Leading to the Next Industrial Revolution, A Report by the Interagency Working Group on Nanoscience, Engineering and Technology (Washington DC: Committee on Technology, National Science and Technology Council), http://www/nano.gov

[7] http://www.rug.nl/research/zernike/education/topmasternanoscience/ns190khikhlovskyi.pdf

[8] Lines and Glass, Ferroelectrics and related materials, Oxford (1977)

[9] http://scholar.lib.vt.edu/theses/available/etd-08062008-102857/unrestricted/Dissertation2.pdf

[10] N. A. Spaldin, S. W. Cheong, and R. Ramesh, Physics Today, P-38, October 2010

[11] Naigang Wang, M.Sc thesis, Material Science and Engineering, Virginia Polytechnic Institute and State University, 2005

[12] H. Schmid, Ferroelectrics, 162, 317 (1994)

[13] G. A. Smolenskii, I. E. Chupis, Ferroelectric magnetic materials, Usp. Fiz. Nauk 137, 415-448 (1982) (in Russian)

[14] Y. Tokura, Colossal Magnetorestive Oxides, Gordon and Breach Science Publishers, Amsterdam, Netherlands, 2000

[15] J. Wang, J. B. Neaton, H. Zheng, V. Nagarajan, S. B. Ogale, B. Liu, D. Viehland, V. Vaithyanathan, D. G. Schlom, U. V. Waghmare, N. A. Spaldin, K. M. Rabe, M. Wuttig, R. Ramesh, 299, 1719-1722, Science 2003

[16] K. Yun, D, Ricinschi, T. Kanashima, M. Noda, M. Okuyama, Jpn. J. Appl. Phys. **2004**, 43, L647-L648

[17] http://cdn.intechopen.com/pdfs/44929/InTech-Optical_properties_of_multiferroic_bifeo3_films.pdf

[18] B. B. van Aken, T. T. M. Palstra, A. Filippetti, & N. A. Spaldin, Nature Mater. **3,** 164–170 (2004)

[19] C. J Fennie, K. M. Rabe, Phys. Rev. B **72,** 100103(R) (2005)

[20] C. Ederer, N. A. Spaldin, Phys. Rev. B **74,** 1 (2006)

[21] S. M. Sze, Physics of Semiconductor Devices, 2nd edn (John Willey & Sons), 1981

[22] Meng Quin, Kui Yao, Yung C. liang, Appl. Phys. Lett. 93, 122904, 2008

[23] S. Y. Yang, et al. Nature Nanotech **5,** 143–147 (2010)

[24] Haitao Huang, Nature photonics, vol 4, March 2010

[25] Q. Meng, Y. Kui, and C. L. Yung, Applied Physics Letters, 93 (12), p.122904 (2008)

[26] Y. S. Yang, S. J. Lee, S. Yi, B. G. Chae, S. H. Lee, H. J. Joo, M. S. Jang, Applied Physics Letters, 76 (6), p. 774-776. (2000)

[27] R. Ramesh, N. Spaldin, Nature Materials, Vol. 6, January (2007)

Chapter 2 Growth Procedure and Characterization Techniques of Thin Films

2.1 Growth technique of thin films

Pulse laser deposition (PLD) of typical perovskite thin films

Pulsed laser deposition (PLD) is a physical vapor deposition process which shares some process characteristics with molecular beam epitaxy (MBE) and some with sputtering deposition. A PLD system consists of a closed high vacuum chamber equipped with the facilities needed for rotating a target containing the material(s) to be deposited, in front of the substrate, on which the film is grown. The physics behind laser-matter interaction, starting from creation of plasma plume to plasma expansion has been described well in reference [1]. A typical PLD system is shown in **Figure 2.1**. A pulsed laser beam with sufficiently high energy density is focused on the surface of the target material. Each laser pulse ablates a small amount of material from the target, creating a plasma plume in front of the surface. The plume expands adiabatically towards the substrate, where the material is deposited. Generating and expanding plasma plume undergoes three consecutive processes: interaction of the laser beam with the target material resulting in evaporation of a thin surface layer, interaction of the evaporated material with the incident laser beam resulting in an isothermal plasma formation and expansion, and anisotropic adiabatic expansion of the plasma leading to the characteristic nature of the laser deposition process [1]. This plume supplies sufficient material to the substrate for film growth. The successful synthesis by PLD of perovskite structured complex oxide material (more specifically high temperature super conductors) has been achieved in the late 1986, and started a new era in film growth techniques. PLD has several characteristics that make it competitive in complex oxide thin film research area as compared to other film growth techniques. The most important advantages of PLD are the stoichiometric transfer of the ablated material from multicomponent target, excited oxidizing species [2], and the simplicity of its set up. Due to these attractive characteristics as a multicomponent film growth technique, a number of applications have been actively pursued for the fabrication of specific structures and devices. Now a day PLD has been widely used in depositing insulators, semiconductors, metals, polymers, and even soft biological materials.

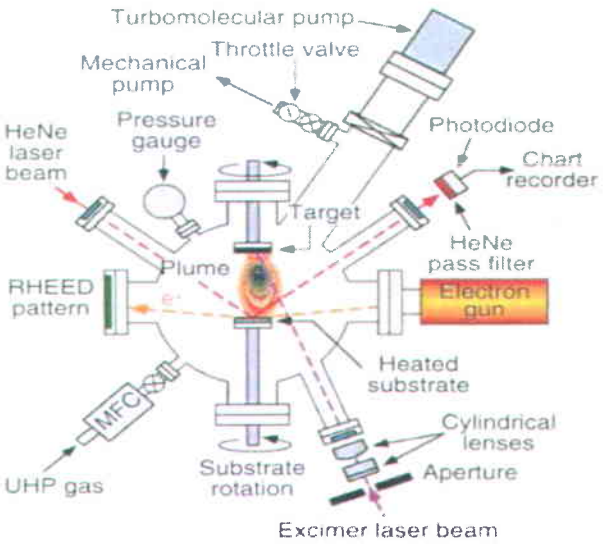

Figure 2.1 Schematic diagram of Pulse Laser Deposition (PLD) [3]

In PLD, there are several parameters that might affect the morphology and crystal quality of thin film. The most fundamental parameters are the vacuum base pressure (~10^{-5}-10^{-10} mbar), the background gas pressure (for most complex oxide materials ~1-100 mbar), substrate temperature during deposition (500-1000^{0}C), laser fluence (1-3 J/cm^2 for most perovskite oxide materials), laser frequency (repetition rate of the pulses, 1-20Hz), the distance between the target material and substrate distance, and laser spot size on the target material. Each and every parameter is interdependent. Changing one parameter affects the deposition rate/growth rate (0.001 to 1 A^0) of the thin film resulting in changing the morphology. On the other hand, there are some other consideration to investigate penetration of growth and film quality that is directly related with the substrate, such as orientation and crystalinity, lattice constant, and whether the surface is singular or vicinal. Depending on the surface free energy of the substrate, three classical growth modes can be distinguished: Frank Van der Merwe, Volmer-Weber and Stranski-Krastanov [4]. Apart from that there are another four epitaxial growth modes that is often used such as step flow mode, columnar growth, step bunching, and screw-island growth.

A particular importance in PLD has the background gas in the chamber at the time of deposition, because it affects the phase formation of the multication system. In complex oxide materials, for example in the case of $BiFeO_3$ film deposition, the background oxygen pressure serves as a reactive species for plasma plume to form the appropriate phase on the substrate,

depending on the thermodynamic stability of that phase. Besides, the background gas reduces the kinetic energy of the species in the plume. This kinetic energy has an important impact on the substrate deformation since high energetic species introduce compressive stress. The compressive stress associated with subsurface damage from the impinging energetic species leads to interstitial defects and thus a lower quality of the resulting film.

It is also crucial to maintain the substrate at the optimum deposition temperature in order to achieve the appropriate phase formation, a condition generally required for any material grown by PLD. A low deposition temperature usually prevents the formation of the crystalline phase of the film. Nonetheless, a deposition temperature above optimum causes inter-diffusion reaction at the interface between film and substrate, or the reconstruction of the substrate surface that strongly alters the physical properties of the as grown films. For instance, if the temperature at the time of deposition of Bi based perovskites is too high, re-evaporation of volatile Bi components from the film occurs, resulting in a film with Bi deficiency. In a nutshell, the kinetics of film growth is partially dependent on the selection of proper temperature.

One of the most important drawbacks of PLD is the formation of micron size particles, called droplets, on the film surface. Droplets are transferred to the substrate when the penetration depth of the laser pulse into the target material is large enough. The use of highly dense target material might reduce droplets but not completely. Therefore, some sort of mechanical techniques have been employed to reduce the droplets, specifically velocity filters, off-axis deposition and line of sight shadow masks [5, 6, 7]. Thickness uniformity of the film when depositing over a large area is another critical challenge of the PLD technique. The highly directional nature of the ablation plume hinders the growth of films with uniform thickness over large area. Recent developments in the design of the PLD system, however, minimize this problem by employing raster scanning of the laser beam over the surface of the target and rotating the substrate.

In this study, we have used a fully equipped PLD system consisting of a GSI Lumonics KrF excimer Laser (λ=248nm with a pulse FWHM τ=15.4 ns) and a vacuum chamber. The chamber is evacuated to reach our required background vacuum pressure (~10^{-5} mbar) by using a mechanical and turbo pump establishing outside of the chamber. The train of laser pulses enters

into an optical system made of mirrors and lenses, then enters the chamber through a quartz window and strikes the target material at an angle of 45^0 from the surface normal. The laser beam is focused such that the impact region (the "laser spot") has the desired size, thus controlling the incident energy density.

A numerical computer control system has been employed to control and measure the laser parameters particularly pulse repetition rate, laser energy and number of laser pulses. The substrate temperature is monitored using a K-type thermocouple during film deposition. The typical deposition temperature was between 580^0 C and 860^0 C depending on requirement. Substrate-target distance has been controlled manually and it was kept constant at 5.5 cm. The calculated laser fluence was in between 1 - 4 J/cm^2 and laser repetition rate was between of 2-8 Hz.

2.2 Characterization Methods

2.2.1 X-ray Diffraction (XRD)

The discovery of X-rays in 1985 by German physicist William Roentgen was the breakthrough of many aspects of science. The immediate application of the X-rays was radiography-widely used nowaday in medical science by physicians. Later on Von Laue et al. in 1912 showed atomic diffraction patterns of crystalline material (zinc sulfide) by X-rays followed in 1914 by English physicist Sir William Henry Bragg and his son Sir William Lawrence Bragg who showed that the scattering of x-rays could be as "reflection" by successive planes of atoms within a crystal. With the arrival of monochromatic X-ray sources, it has further been shown that a periodic arrangement of atoms in a crystal leads to the diffraction of X-rays. The intensity of the diffracted wave might be maximum or minimum depending on the type of interference. Constructive interference of scattered photons leads to high intensity.

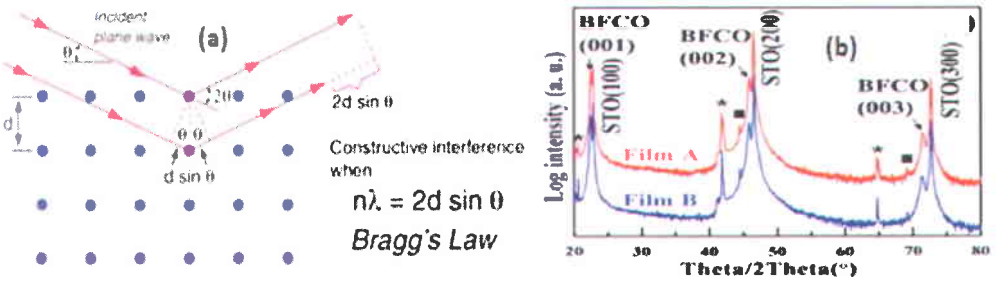

Figure 2.2 (a) Schematics of diffraction of X-rays by periodic arrangement of planes of atoms [8] (b) example of diffraction pattern obtained for Bi_2FeCrO_6 (BFCO) thin film deposited on (001) oriented $SrTiO_3$ substrate showing the single crystallinity of BFCO [9]

This is shown clearly in **Figure 2.2 (a)** which illustrates the working principle of XRD. Geometrically, the distance between two parallel planes of periodically arranged planes (d), the wavelength of a monochromatic X-ray source (λ) and the diffraction angle (θ) are being correlated with each other by the following equation known as Bragg's law, $n\lambda=2dsin\theta$, where n is the order of reflection. Since the wavelength (λ) is about equal to the distance between two atoms (approx. *0-5* A^0), the XRD technique is an extremely powerful tool for measuring crystalline structure of a given material.

The experimental setup for performing an XRD experiment is very simple in nature. A beam of X-rays from a monochromatic X-ray source is focused on the sample, under a precise incident angle. This sample is fixed on the movable flat plate. The diffracted beam from the sample is then collected in an X-ray detector, which gives a signal proportional to the number of photons along the sample-detector direction. This signal is then recorded as a function of 2θ (see Fig. 2.2). Each parallel set of crystalline planes of the investigated sample produce an unique diffracted pattern. This pattern is then compared with a library of standard patterns (in X'Pert High Score) of specific structure of elements as well as compounds. Finally, a set of information about such as crystalline structure, crystallite size distribution, and lattice parameter has been extracted by analyzing angular the position of the recorded diffracted peak maximum, amplitude and width of the peak. **Figure 2.2 (b)** shows an example of typical XRD data.

We used a high quality XRD system, namely the High resolution PANalyticalX'Pert Pro MRD 4-circle diffractometer system. This system gives us facilities to do a lot of measurements

such as phase analysis in θ-2θ (Bragg-Brentano), grazing incidence, Phi scan measurement to test the epitaxial deposition, texture analysis, high resolution reciprocal space mapping, high resolution rocking curve measurement, residual stress analysis and X-ray reflectivity measurement. In our study, we used extensively θ-2θ and grazing incidence measurement to realize the structure and quality of the as-deposited thin films. In addition, using X-ray reflectivity measurements we assessed the thickness of the as-prepared films.

2.2.2 Electron Microscopy (EM)

Conventional light microscopy (LM) uses visible light of wavelengths from about 400 nm to 700 nm with a resolution of 0.2 microns (μ) as a source of illumination and optical lenses to magnify the sample. In contrast, electron microscopy (EM) uses a high energetic focused electron beam in a vacuum to investigate an object on a very fine scale. The advantage of EM over light microscopy consists in the very short wavelength associated to electrons (λ=0.005nm at an accelerating voltage of 50KV) with a resolution of about 25 angstrom (A^0) that, in principle, enables atomic scale resolution. It uses electromagnetic lenses to magnify the specimen. EM yields information about the topography (surface features of an object), morphology (shape and size of the particles making up the object), composition (the elements and compounds that the object is composed of and the relative amounts of them) and crystallographic information (how the atoms are arranged in the object) [10].

The basic research on electron microscopy has been started in 1920's when the properties of accelerated electrons (wavelike properties with shorter wavelength than visible light) in vacuum have been discovered. As a consequence of the progress of research, in 1931, Max Knoll and Ernst Ruska constructed a two stage electron microscope with three magnetic lenses, condenser, objective, and projector [11], known as the first Transmission Electron Microscope (TEM). Later on in 1938, Manfred von Ardenne invented another type of electron microscopy based on the scanning of an electron beam over a sample and they called their system scanning electron microscope (SEM) [12].

An electron microscope consists of an electron optical column, a vacuum system, electronics and software. All these function together obtains a good image of specimen. In principle, when a sample is bombarded with an incident electron beam, there might occur two

types of collisions: elastic and inelastic, which produce backscattered electrons, secondary electrons, Auger electrons, characteristic X-rays and cathodoluminescence. Based on these emitted electrons, two basic types of electron microscopes exist, namely Scanning electron microscope (SEM) and Transmission electron microscope (TEM) that are briefly explained below.

Scanning Electron Microscopy (SEM)

Scanning electron microscopy (SEM) uses a focused electron beam that rasters over the surface of the sample in vacuum to extract structural and chemical information point-by-point from a region of interest in the sample. The high spatial resolution of an SEM makes it a powerful tool to characterize a wide range of specimens at the nanometer to micrometer length scales [13]. Scan coils and objective lens shown in **Figure 2.3 (a)** are used to deflect the electron beam horizontally and vertically in order to achieve a proper scanning over the surface of the specimen. Based on the type of electron scattering, a reasonable amount of emitted electrons is collected by appropriate detectors. The output of these detectors is synchronized with the x-y input of the cathode ray tube (CRT) where images are formed, according to the x-y beam deflection on the surface. The following equation denotes linear magnification, M=L/l, where 'L' is the scanning length of the CRT monitor and 'l' the scanning length on the surface of the specimen.

The typical beam diameter of the SEM is between 5 nm to 2μm and the working (accelerating) voltage is from 2 to 50 KV. SEM deals with basically three types of signals: secondary electrons, backscattered electrons, and elemental electrons. In SEM, secondary and backscattered electron signals are used for the visualization of the surface of a specimen. Secondary electrons, a result of inelastic collisions, are used to image the surface structure of a sample with the resolution of 10 nm or better. Nevertheless, backscattered electrons, a result of elastic collision, help to resolve topographical contrast and atomic number contrast with a lateral resolution better than 1 micron. While secondary electron imaging infers energy of the emitted electrons below 50 eV, the backscattered electrons have an energy greater than 50 eV [14]. The limitations of SEM are that it can only deal with conductive specimens and gives only surface

image. In addition, it cannot detect those materials which have atomic number smaller than that of carbon.

Transmission Electron Microscopy (TEM)

When a beam of electrons passes through a crystalline specimen, it is scattered according to the Bragg's law. The scattered beams at small angles are focused by the objective lens to form a diffraction pattern at its back focal plane. The scattered beams are recombined to form an image in the image plane [15]. **Figure 2.3 (b)** shows a typical schematic of a TEM. In the case of diffraction patterns, the whole illuminated area of sample generates electrons, and, in order to protect the screen, a virtual image of the specimen is produced by placing a small aperture in the image plane of the objective lens. The pattern obtained by placing this aperture is called selected area diffraction (SAD). TEM gives two types of imaging of a sample, depending on whether direct electron transmission or scattered electrons are involved. If the directly transmitted electron beam is used, the image obtained is referred to as the bright-field image, while the scattered electron beam results in the so-called dark-field imaging.

TEM provides information about the crystalline structure of the specimen by showing different types of diffraction patterns such as dots, regions or circles that originate from the irradiated area of the sample. Dotted, center-circled and diffuse-circled diffraction pattern indicates mono-crystalline, polycrystalline and amorphous structure of the specimen, respectively.

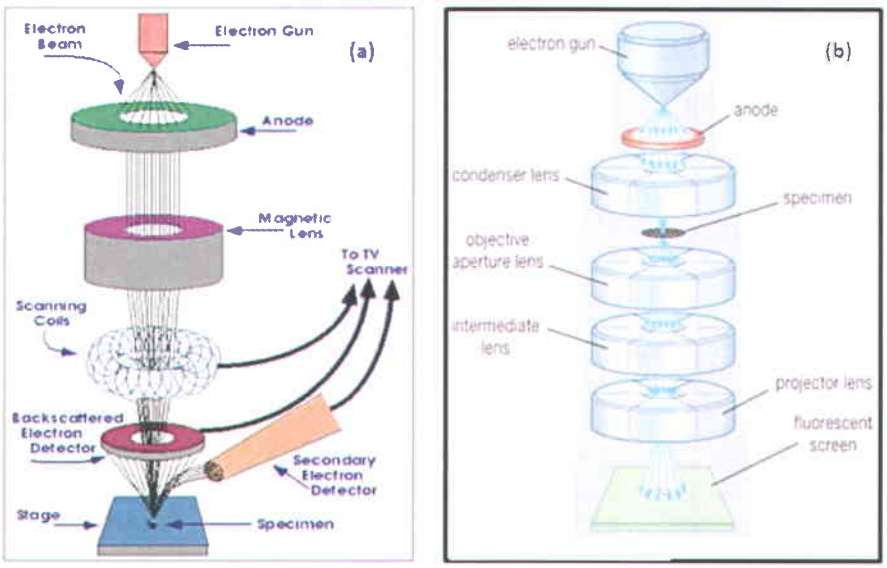

Figure 2.3 Schematics of a typical Scanning Electron Microscope (SEM) (a) [10] and Transmission Electron Microscope (TEM) (b) [10]

2.2.3 Scanning Probe Microscopy (SPM)

The probe-based microscopies, referred to as SPMs, have been developed since the discovery of Scanning Tunneling Microscopy (STM) and Atomic Force Microscopy (AFM) in 1982 by Gerd Binning and H. Rohrer, and 1985 by Binning et al respectively. SPMs allow investigation and manipulation of a specimen surface down to the atomic scale and thus it is associated with nanoscale science and technology. SPMs enable sharp imaging of sample surface by means of measure a local physical quantity related to the interaction between a sharp probe (tip) and the surface of the sample. Dedicated software and electronics process all the extracted data in order to render an image of the surface of the specimen. Due to their astounding capability to probe tip-sample interactions, SPMs have become of increasing interest for imaging electronic, magnetic, biological, and chemical properties at the surface of various specimens. In our work, we used two basic scanning probe microscopes, named atomic force microscopy (AFM) and piezoresponse force microscopy (PFM). They are briefly discussed below.

Atomic Force Microscopy (AFM)

The fundamental working principle of AFM relies on the measurement of the forces between a sharp fine tip and a sample. The tip is typically attached to the free end of a flexible cantilever and is brought in the proximity of the sample surface. The force acting on the tip is transmitted to the cantilever, which deflects a laser beam reflected off from its back onto a segmented photodiode that gives signals which can be used to obtain the deflection of cantilever. Therefore, the interaction force can be monitored/controlled, and, by doing this while the tip is rastered across the surface, the sample topography can be retrieved. **Figure 2.4 (a)** shows the schematics of the general working procedure of all SPMs.

There are three modes of operation of an AFM: contact mode, non-contact mode and tapping mode (intermittent contact mode). **Figure 2.4 (b)** shows a force vs distance curve indicating the three modes of operation. In contact mode operation, the tip makes a soft physical contact with the sample while scans over the sample by maintaining either a constant small height (less than a few angstrom) or under a constant force (van der Waals force, capillary force and force extracted by the cantilever itself). It yields atomic scale of resolution with high scan speed but might distort the image because of lateral force of cantilever. In non-contact mode, the tip scans while maintaining a sufficient distance (approximately at least one nanometer) from the sample surface and operates in the attractive force region of the figure. This mode prevents breakage of soft sample but yields lower lateral resolution due to tip-sample separation. In tapping mode, the cantilever oscillates close to its resonance frequency and the tip touches the scanning surface only for a fraction of its oscillation period. An electronic feedback loop ensures a constant oscillation amplitude by adjusting the tip-sample separation. Despite of its slower scan speed, tapping mode operation presents high lateral resolution (1nm to 5 nm) of the tested sample.

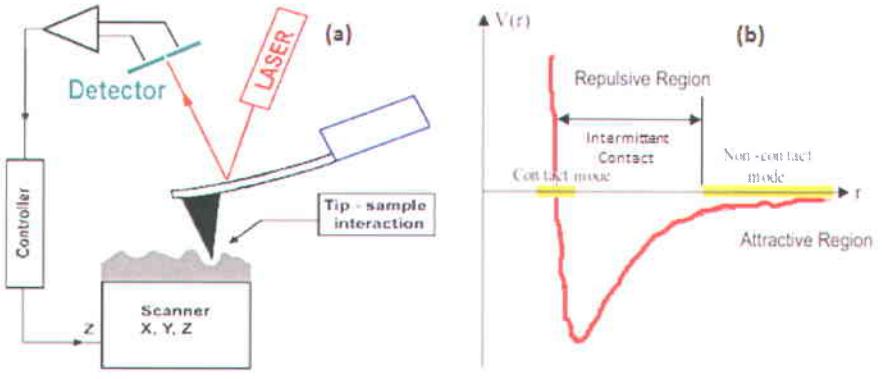

Figure 2.4 (a) working principle of AFM technique (b) Force- distance curve plotted as a function of tip distance from the sample [16]

In our work, we have used AFM measurements to characterize the surface of the as-grown films using Veeco DI-EnviroScope microscope. Tapping mode operation of AFM has been selected to make an image of surface topography.

Piezoresponse Force Microscopy (PFM)

PFM is a versatile tool for the detection and imaging of ferroelectric domains at nanoscale, based on the converse ferroelectric effect. In PFM, the signal originates in the deformation of the ferroelectric material upon applying a small electric field. **Figure 2.5** shows a typical PFM image and explains the imaging principle of PFM, where an applied alternating voltage on the conductive AFM tip creates an electric field in the sample. Depending on the parallel or perpendicular direction of polarization with respect to this electric field, PFM detects and creates an image of either out of plane (z-PFM) or in plane (x-PFM) polarization, respectively.

Extracting the induced sample oscillations of the sample surface is a complex process. To do it, a lock-in system is employed that eliminates the noise together with all harmonic components from the actual deflection signal. The remaining signal thus represents only the sample response, and is referred to as piezo response signal.

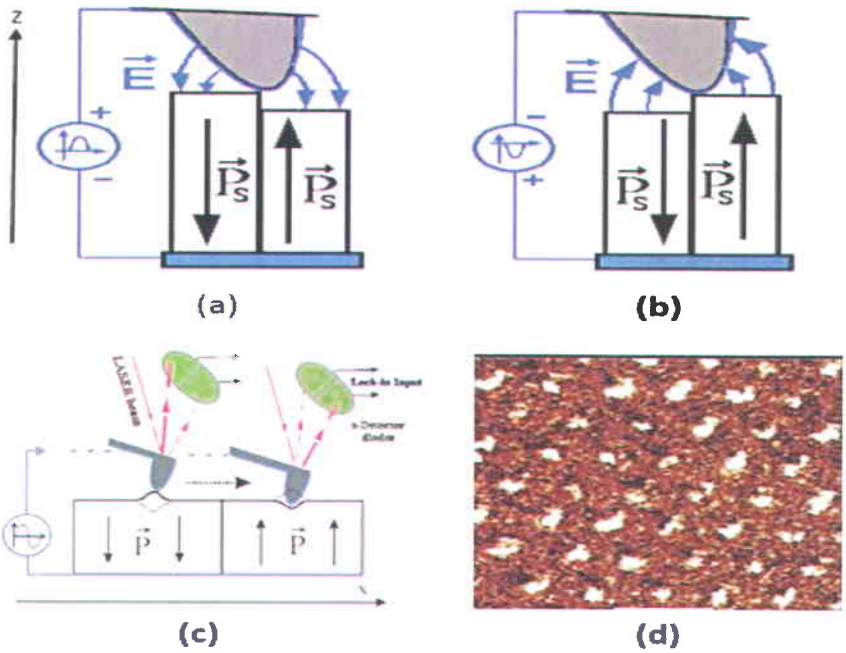

Figure 2.5 (a) and (b) Schematics of changing thickness by applying positive and negative half cycle of ac voltage respectively [16] (c) Schematics of the detection of piezo response signal [16] (d) x-PFM image of Bi_2FeCrO_6 epitaxial pattering [17]

In our experiment, we used the same commercially available instrument, the Veeco DI-Enviroscope, equipped with a computer controlled lock-in amplifier (Signal Recovery model 7265). In this instrument, the cantilever axis is contained in the plane of the laser beam. A conductive silicon cantilever coated with Co-Cr (NSC 36/Co-Cr) was used for applying the AC voltage. The silicon cantilever is highly doped, and its resonance frequency and spring constant are 68.68 KHz and 0.5 N/m, respectively. The amplitude of the applied AC voltage was in the range from 0.5V to 1V. Hysteresis loop measurements were performed using a computer controlled Keithley 2400 Digital SourceMeter (Cleveland, OH) which supplied the DC voltage (-5V to +5V), connected in series with the AC source.

2.2.4 X-ray Photoemission Spectroscopy (XPS)

X-ray photoelectron spectroscopy (XPS), also known as electron spectroscopy for chemical analysis (ESCA), is one of a number of surface analytical techniques that bombard the sample with photons, electrons or ions in order to excite the emission of photons, electrons or ions [18]. In

XPS, the sample is irradiated with low-energy (~1.5 keV) X-rays and measures energy spectrum of the emitted photoelectrons to obtain quantitative analysis of the surface by means of a high-resolution electron spectrometer. The high resolution beta ray XPS was developed in 1960s by the several significant improvements in the equipment by the group of K. M. Siegbahn. In recognition of his extensive efforts to develop XPS into a useful surface analytical tool, Siegbahn was awarded half of the Nobel Prize for Physics in 1981 'for his contribution to the development of high resolution electron spectroscopy'[19]. The sample analysis is conducted in a vacuum chamber, under the best vacuum conditions achievable, typically ~10^{-10} torr. This facilitates the transmission of the photoelectrons to the analyzer but more importantly minimizes the re-contamination rate of a freshly cleaned sample. This is crucial because XPS is very surface-sensitive, with a typical "sampling depth" of only a few nanometers.

A typical XPS spectrum is obtained by recording the number of emitted photoelectrons as a function of the binding energy. The energy of the photoelectrons basically characterize the element and configure the electrons inside the atom such as 1s, 2s, 2p, 3s etc. The basis of XPS experiment is to determine the kinetic energy of photoelectrons. It can be determined by following equation: $E_k=h\gamma-E_B-\Phi$ where $h\gamma$ is the photon energy of the X-ray source, *EB* is the binding energy of the atomic orbital from which the electron originates, Φ is the spectrometer work function. The intensity of the XPS characteristic peaks correspond to the amount of element within the area or volume probed. Thus XPS yields information about the elemental composition of the surface, the empirical formula of pure materials, and chemical and electronic state of the elements in the surface and the thickness of thin film on a different substrate within the probing depth (~10 nm of the surface).

2.2.5 Spectroscopic Ellipsometry

Ellipsometry is generally a non-invasive and non-destructive optical technique used for the measurement of the optical properties of a sample material. The principle of this technique is based on the change of the polarization state of light after reflection at oblique incidence on the surface under study. The measurement gives two independent parameters, ψ and Δ, which gives all relevant information about the polarization state of light at a given wavelength. 'Ψ' indicates the rate of amplitude of Fresnel coefficients r_p and r_s for the polarized light waves parallel with

the plane of incidence 'p' and perpendicular to plane of incidence 's'. 'Δ' represents the phase difference between the above mentioned planes p and s, shown in **Figure 2.6.** It does not depend on the absolute intensity as long as it is sufficient. This makes any measurement very precise and reproducible.

Here in our application, we used a new type of ellipsometry measurement named Variable Angle Spectroscopic Ellipsometry (VASE). It gives more comprehensive results since it studies materials over a wide spectral range. The main ellipsometric parameter, ψ and Δ are measured here by changing the wavelength of light guided by inbuilt VASE software. The incident angle of light is varied according to the optical constant of the sample in order to maximize the sensitivity of the measurement. However, there are two general limitations of spectroscopic ellipsometry measurement: the error increases if surface roughness goes above around 30% of the probe wavelength although it is completely dependent on the instrument type; and measurement must be done at oblique incidence, since otherwise (at normal incidence) it is very difficult, kind of impossible, to distinguish the 'p' and 's' planes [120]. The most crucial aspect of VASE ellipsometry is that it is an indirect characterization technique. Therefore, additional optical model with predefined optical constants and sample layer thickness is required to analyze data. WVASE 32 software package of our instrument in this case stores a data base of refractive index for large number of materials.

Additionally, data analysis becomes difficult for the case of very thin film (< 10 nm) because of the difficulties of distinguishing between film and substrate. In addition, small absorption coefficient ($\alpha < 100$ cm^{-1}), the surface roughness (higher value leads to depolarization), transparency of the films, films with high absorption, isotropic and anisotropic structure and many phases in the sample, further makes the characterization difficult. Therefore, another application called effective medium approximation (EMA) is added as optimization to obtain a minimum error.

Spectroscopic Ellipsometry allows measurements with a lateral resolution of ~ 100 microns to millimeters in lateral size, and it makes possible to measure a thickness of a layer of the sample of up to 50 μm. It also gives the extinction coefficient (k) as a function of wavelength (λ)

to measure the attenuation of light in the material. This technique enables additional characterization followed by surface and interface, and layer inhomogeneity.

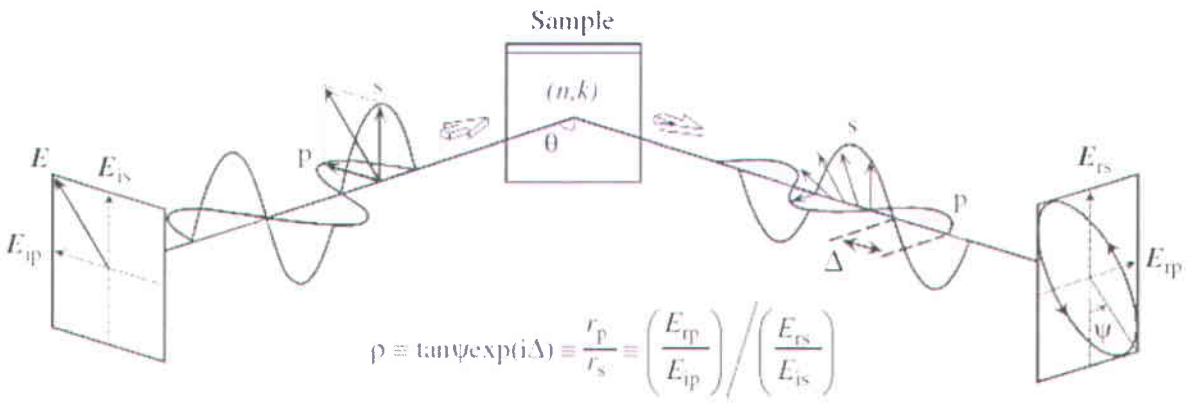

Figure 2.6 Schematic of the principle of Reflection Ellipsometry measurement [21]

2.2.6 Solar Simulator (AM 1.5)

Radiation from the sun sustains life on the earth. The spectrum of radiation from the sun is somewhat similar to the blackbody radiation (5800k). The spectrum of solar radiation outside the earth's atmosphere is denominated as extraterrestrial. Once the spectrum enters into the earth's atmosphere it becomes terrestrial. Several factors affect the terrestrial spectrum such as location, atmospheric condition (cloud, aerosol content in the air, and ozone layer), distance between earth and sun, time of the day etc. Due to the large number of the involved variables on terrestrial solar spectrum, a standard spectrum has been developed to provide a basis for theoretical evaluation of the effects of solar radiation and as a basis for simulator design. The mostly used and accepted standard spectra are those published by The Committee Internationale d'Eclaraige (CIE), the world authority on radiometric and photometric nomenclature and standards. Depending on the tilting of earth's surface, The American Society for Testing and Materials (ASTM) publish three spectra, AM0, AM1.5 Direct and AM1.5 Global. Those spectra maintain a particular standard, for example, ASTM E490, ASTM E891, ASTM E892, ASTM E927, and CIE pub.85 and 904-3. **Figure 2.7** gives a physical meaning and visualization of those spectra.

Here in our experiment we used SS50AAA solar simulator (class AAA) which consists of a high pressure Xenon Lamp (Xenon Short Arc) with 150 W power and a builtin touch panel color

display system controller. Matching the sun's spectra of AM 1.5 G, the output power of the system on the sample located on the flat surface is 100mW/cm^2 (with an error of +/- 15%). Solar spectra of our system is matched to American Society for Testing and Materials (ASTM) E927 standard (with the error of +/- 25%). The life time of lamp is 1000 hours. The system provides controls on the intensity of Xenon lamp having additional shutter controlling the steady state light source.

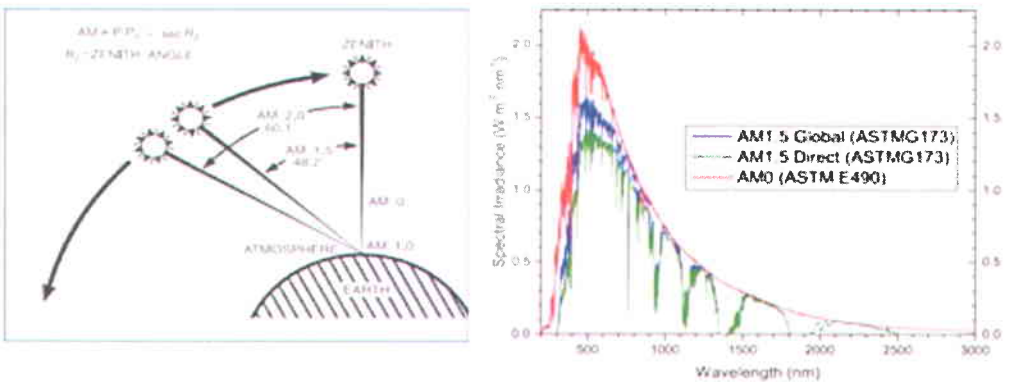

Figure 2.7 (a) Definition of standard spectra [21] and (b) Schematics of typical spectra [22]

2.3 References

[1] Rajiv K. Singh and J. Narayan, Phys. Rev. B 41,13,1990

[2] R. Eason, Pulse Laser Deposition of Thin Films: Applications-Led Growth of Functional Materials, John Wiley & Sons, Inc, 2007

[3] Douglas H. Lowndes, D.B. Geohegan, A. A.Puretzky, D. P. Norton, C. M. Rouleau, American Association for the Advancement of Science, 273, 1996

[4] E. Bauer. Z. Kristallogr, 110, 372 (1958)

[5] B. Holzapfel, B. Roas, L. Schulz, P. Bauer, and G. Saemann-Ischenko, Appl. Phys. Lett. 61, 3178, 1992

[6] E. V. Pechen, A. V. Varlashkin, S. I. Krasnosvobodtsev, B. Brunner and K. F. Renk, Appl. Phys. Lett. 66, 2292, 1995

[7] Z. Trajanovic, S. Choopun, R. P. Sharma, and T. Venkatesan, Appl. Phys. Lett. 70, 3461–3463, 1997

[8] http://hyperphysics.phy-astr.gsu.edu/hbase/quantum/bragg.html

[9] R. Nechache, C. Harnagea, S. Licoccia, E. Traversa, A. Ruediger, A. Pignolet and F. Rosei, Appl. Phys. Lett. 98, 202902, 2011

[10] http://www.mansic.eu/documents/PAM1/Giannakopoulos1.pdf

[11] F. Haguenau, P. W. Hawkes, J. L. Hutchison, B. Satiat-Jeunemaître, G. T. Simon and D. B. williams, Microscopy and Microanalysis **9**, 96 (2003)

[12] F. Haguenau, P. W. Hawkes, J. L. Hutchison, B. Satiat-Jeunemaître, G. T. Simon and D. B. williams, Microscopy and Microanalysis **9**, 96 (2003)

[13] B. Holzapfel, B. Roas, L.Schulz, P. Bauer, and G. Saemann-Ischenko, Appl. Phys. Lett. 61, 3178, 1992

[14] http://www.mansic.eu/documents/PAM1/Giannakopoulos1.pdf

[15] http://www.mansic.eu/documents/PAM1/Giannakopoulos2.pdf

[16] http://sundoc.bibliothek.uni-halle.de/diss-online/01/01H318/

[17] Riad Nechache , Cristian Victor Cojocaru, Catalin Harnagea, Christian Nauenheim, Mischa Nicklaus, Andreas Ruediger, Federico Rosei, and Alain Pignolet, Adv. Mater. 2011, 23, 1724–1729

[18] http://goliath.inrs-emt.uquebec.ca/surfsci

[19] http://www.nobelprize.org/nobel_prizes/physics/laureates/1981/

[20] R. Pascu, M. Dinescu, Romanian Reports in Physics, Vol. 64, No. 1, P. 135–142, 2012

[21] Hiroyuki Fujiwara, Spectroscopic Ellipsometry Principles and Applications, John Wiley & Sons Ltd, 2007

[22] http://pveducation.org/pvcdrom/appendicies/standard-solar-spectra

Chapter 3 Photovoltaic Properties of $BiFeO_3/BiCrO_3$ Bilayer Hetero-structure

3.1 Introduction

Recently, an encouraging power conversion efficiency, as briefly mentioned earlier, of about 6% under red light illumination (wavelength of 635 nm) in multiferroic epitaxial Bi_2FeCrO_6 (BFCO) thin films[1] and a 10% external quantum efficiency in multiferroic $BiFeO_3$ (BFO) thin films have been reported.[2] Furthermore, V_{oc} values of 15-28 V, which largely exceed the material bandgap (i.e. 2.75 eV), can be produced in BFO thin films[3] and crystals.[4] High short-circuit current density (J_{sc}) of 0.99 mA/cm^2 has been only observed in BFCO thin films, where its magnitude is related to the Fe-Cr cationic ordering. Recently, a combination of BFO and BCO films demonstrated interesting properties: heteroepitaxial BFO/BCO bilayers showed good ferroelectric and enhanced magnetic properties due to the interfacial magnetic coupling between Fe and Cr ions.[5] In addition, room temperature multiferroic properties were observed in artificial BFO/BCO superlattices by Ichikawa et al.[6] It would thus be interesting to investigate the effect of such interface and PV conversion performance of BFO/BCO heterostructures. Variation of the key-parameters such as thickness (x) and number (y) of BFO and BCO bilayers will be helpful to understand the mechanism underlying the PV effect observed in multiferroic thin films.

Here, we report the PV properties of periodic multi-stacking of BFO/BCO bilayers epitaxially deposited on $CaRuO_3$ (CRO) coated $LaAlO_3$ (LAO) substrates by pulsed laser deposition (PLD). The as prepared heterostructure exhibits significant light to electrical power conversion efficiencies compared to the efficiencies of the contributing single layers BFO so far reported until now. A large photo voltage, V_{oc} is observed when the number of BFO/BCO stacking is increased in the structure. Maximum photocurrent is generated at an optimal multilayer thickness of 60 nm, where its origin is mainly due to ferroelectric polarization contribution.

3.2 Multilayer Films Growth

Heteroepitaxial BFO/BCO structures were grown on $CaRuO_3$ (CRO) coated (100)-oriented LAO substrate by PLD sequentially. First, CRO films were deposited on LAO substrate by maintaining the following PLD growth parameters: T_s=610^{0}C, P_{O2}= 20 mTorr. CRO layer will serve as bottom electrode to perform electrical measurements. Keeping temperature of substrate at 700^0 C and pressure of oxygen at 8 mTorr, BCO film were deposited on CRO coated LAO substrate. Finally, at the time of BFO film growth, substrate temperature and background pressure of oxygen were of 620^0 C and 25mTorr respectively. Respective growth conditions were kept for subsequent growth of other deposited films. All films were cooled down to room temperature at a slow rate of 10 °C/min in 300 mTorr of oxygen.

3.3 Experimental Results

3.3.1 Structure and Morphology

3.3.1.1 XRD Analysis

The single phase structure of the BFO/BCO multilayers is evidenced using X-ray diffraction (XRD). As shown in **Figure 3.1**, the θ–2θ scan have no indication of the presence of additional phases other than (001) oriented layers. In all prepared heterostructures, the reflections from BFO and BCO phases are clearly distinguished in the XRD spectra even for the structure with the highest number of bilayers. XRD spectra exhibit however split BFO (00l) reflections, which suggests the appearance of strain inhomogeneity in the heterostructure with increasing thickness.

The significant lattice mismatch between BFO and BCO with respect to LAO (3.792 Å) induces a considerable strain in the epitaxial grown BFO and BCO films. This strain stabilizes the single phase of each material in a tetragonal structure.[7]

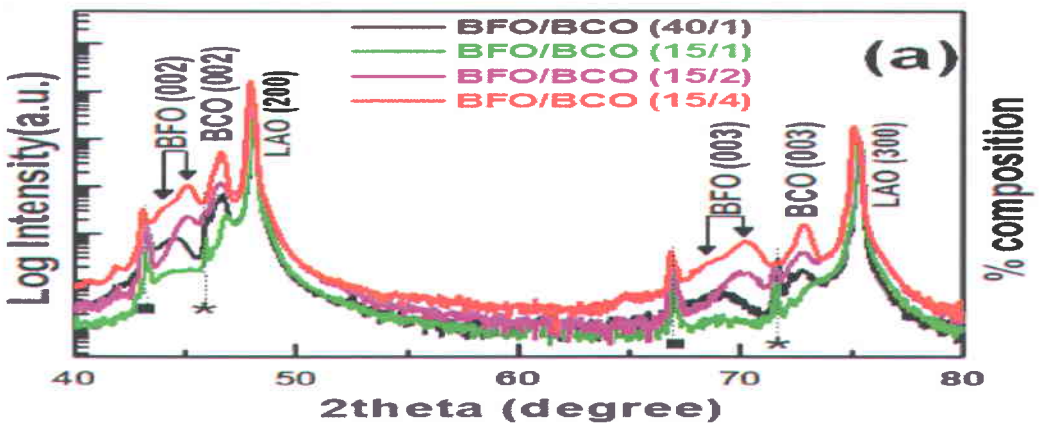

Figure 3.1 XRD θ-2θ scans of BFO/BCO/CRO heteroepitaxial thin films grown on (100) oriented LAO substrate. x and y in BFO-BCO (x/y) formula represent the thickness (nm) and number of layer respectively. Squares and stars correspond to K_β and tungsten contamination contributions, respectively.

3.3.1.2 TEM Analysis

Figure 3.2 (*a*) and (b) shows a typical cross-sectional high-resolution Transmission Electron microscopy (HRTEM) images of as-grown heterostructure deposited on (100) oriented CRO coated LAO substrate. They confirm the epitaxial growth and good crystal quality of individual layer involved in the heterostructure. In addition, **Figure 3.2 (c), (d), (e)** and **(f)** shows diffraction pattern of corresponding fast fourier transform of each layer. The sharp diffraction spots of each layer prove their well-developed single crystalline structure which is in good agreement with studied XRD spectrum in the above mentioned text.

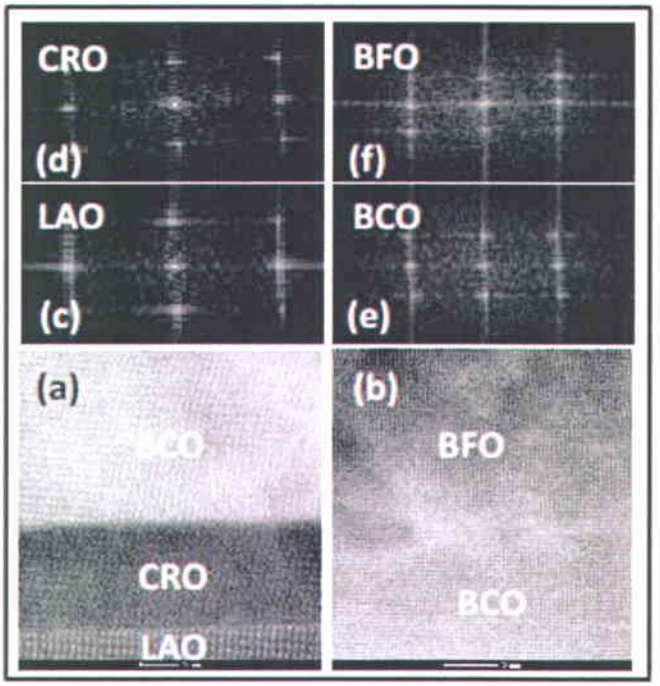

Figure 3.2 High resolution TEM images of heterostructure (a) and (b), with corresponding fast fourier transform (c), (d), (e) and (f) of each layer individually

Figure 3.3 illustrates a typical Electron dispersive X-ray (EDX) spectrum in TEM of BFO/BCO (40/1) heterostructure where intermixing at interfaces is observed. The estimated interlayer thicknesses are 9.1 nm, 7.5 nm and 5.7 nm at BFO/BCO, BCO/CRO and CRO/LAO interfaces, respectively (within an experimental error of 5%).

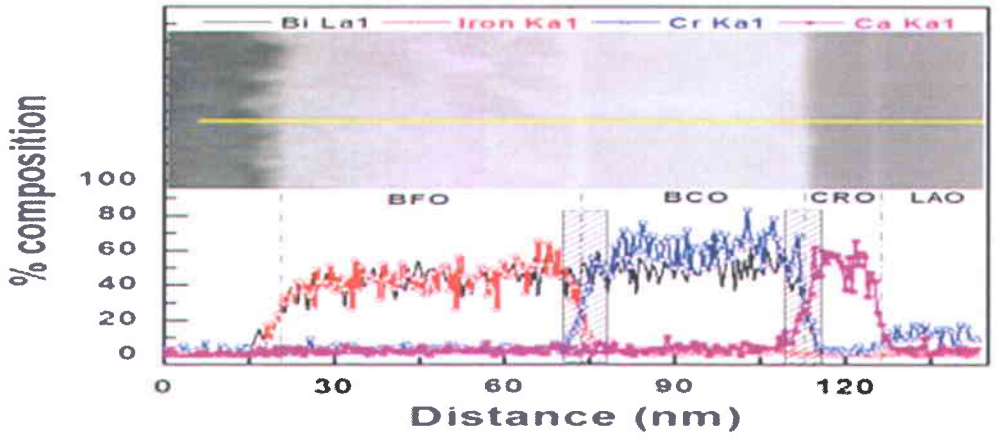

Figure 3.3 EDX spectra of as deposited BFO/BCO/CRO heterostructure. The inset displays the corresponding low magnification cross-sectional TEM image of the heterostructure.

3.3.2 AFM Study: Surface Analysis

A typical AFM surface topography of bottom BCO film is illustrated in Figure 3.4 (a). AFM imaging shows that this film is characterized by a rough surface with r.m.s. and peak to-valley values of 1.5 nm and 4.5 nm, respectively as shown in Figure 3.4 (b). The heterostructure surface remains rough even after BFO layer deposition as illustrated in Figure 3.4 (c). Such surfaces might contribute to the interface mixing, in particular when 2D film growth conditions are not reached as schematically represented in Figure 3.4 (d).

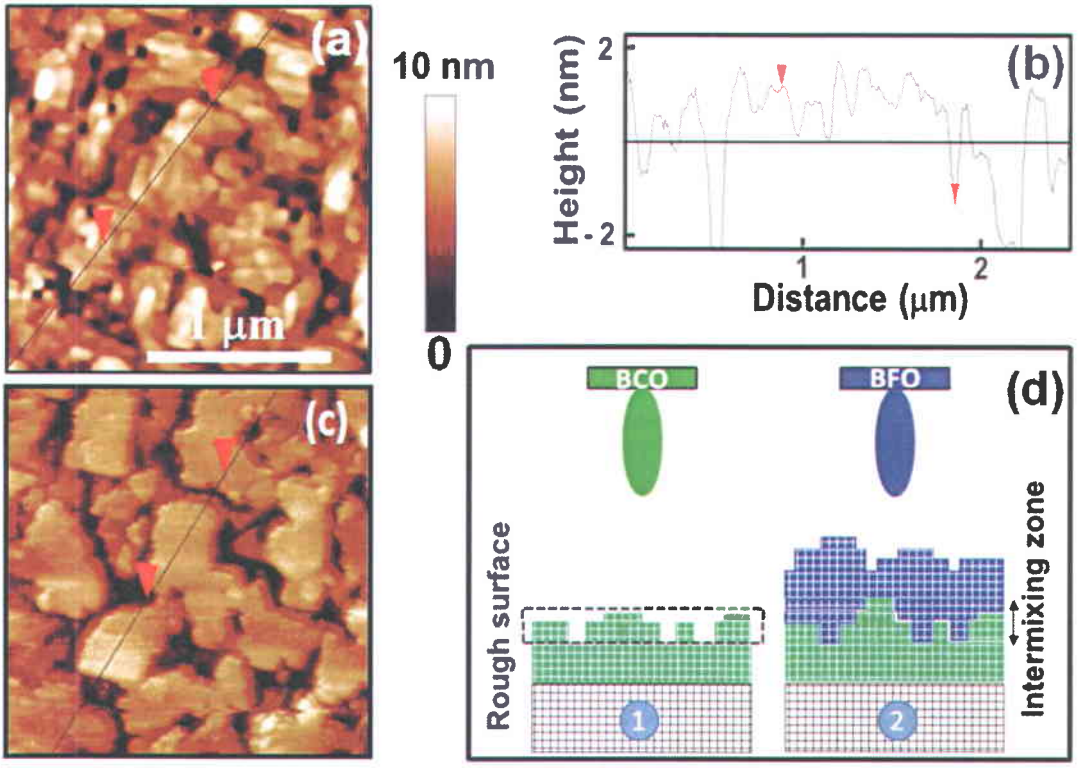

Figure 3.4 (a) (2 x2 µm) AFM image of the BCO/CRO/LAO surface and (b) corresponding surface profile analysis. (c) AFM image of same sample after the deposition of BFO layer. (d) Schematic representation illustrating the intermixing phenomenon observed during BFO/BCO bilayer deposition. The part of the scheme labeled (1) refers to the growth of BCO film characterized by a rough surface and those labeled (2) show the sequential deposition of BFO with the formation of an intermixing zone.

3.3.3 Current Density (J)-Voltage (V) measurement of proposed device geometry

The PV properties of the BFO/BCO heterostructures were investigated by performing current (*I*)-voltage (*V*) measurements both in dark and under sun simulator with maximum power density of 100 mW/cm^2 (AM 1.5 filter). The measurements were performed in both unpoled and then in poled condition by applying appropriate potential between top and bottom electrodes. Two dimensional arrays of Indium Tin Oxide (ITO) films deposited by PLD through a shadow mask were used as top electrodes, shown in Figure 3.5 (a).

The geometry of the tested structures and current density (J)-voltage (V) curves of all samples are shown in Figure 3.5. Among them, the sample with four alternating, each layer of 15 nm thick BFO/BCO bilayers [i.e. BFO/BCO (15/4)] exhibits the highest V_{oc} (~1.2V) which decreases linearly in magnitude as the number of incorporation of bilayers is reduced in the structure (cf. Fig. 6a). Most importantly, the small J_{sc} value observed for the single bilayer [BFO/BCO (40/1)] becomes more significant when the layer thickness is reduced [BFO/BCO (15/1)]. The highest J_{sc} value of ~0.015 mA/cm^2 is recorded in the two alternating 15 nm-thick BFO/BCO bilayers [BFO/BCO (15/2)].

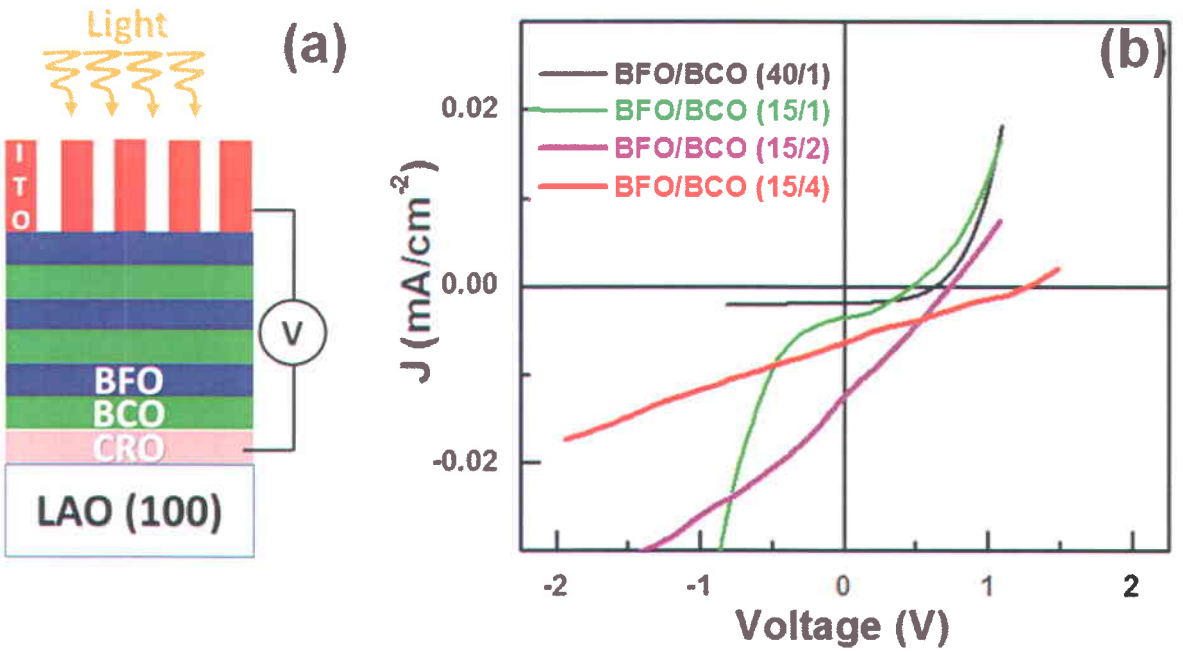

Figure 3.5 (a) Geometry of tested structure involving BFO/BCO bilayers. (b) J-V measurement curves revealing PV effect in BFO/BCO heteroepitaxial films.

3.3.4 Ferroelectric Switching of J-V Curve

There are two likely scenarios that can explain the origin of the experimentally observed PV effect. The first one is the effect of the Schottky barrier at electrode–film interface that would depend on the alignment of Fermi level and second is the effect of ferroelectric polarization induced electric field in the film. The formation of schottky barrier at ITO-BFO interface could separate photo charge carrier effectively.[9] The second involves the role of the ferroelectric

polarization as a driving force for charge separation within the device. Therefore, the PV effect comes from the combined effect of polarization induced internal electric field plus interface schottky barrier induced internal field. In order to estimate the contribution of ferroelectric polarization to PV effect in our J-V measurement curve conducted on BFO/BCO (15/4) sample, we used a microsecond pulse of ±15V to get alternative positive and negative poling of the film respectively. After each poling, J-V measurement was performed, shown in **Figure 3.6** (b). The red curve in **Figure 3.6** (b) shows that the value of short circuit photo current as well as photo voltage is increased compared with the observed photo current and photo voltage in **Figure 3.6** (b). This improvement of the photo current and photo voltage taken after polarization switching is attributed to a higher degree of domain alignment.[8] The as-grown heterostructures exhibit no preferential ferroelectric domain orientations (cf. right inset of **Figure 3.6** b) as revealed by Piezoresponse force microscopy (z-PFM). At local scale the ferroelectric domains can be locally switched by applying ± 5V voltage pulses. However, in macroscopic measurement, the film became down poled after applying a -15 V pulse. On this condition, the polarization directs towards the bottom electrode (connected with substrate) and the depolarized field (E_{dp}) directs toward the top electrode.[9] As a result, a negative J_{sc} (~ 0.013 mA/cm^2) was recorded. The reverse phenomenon was observed after applying +15 V pulses and measuring a positive J_{sc} around ~0.008 mA/cm^2.

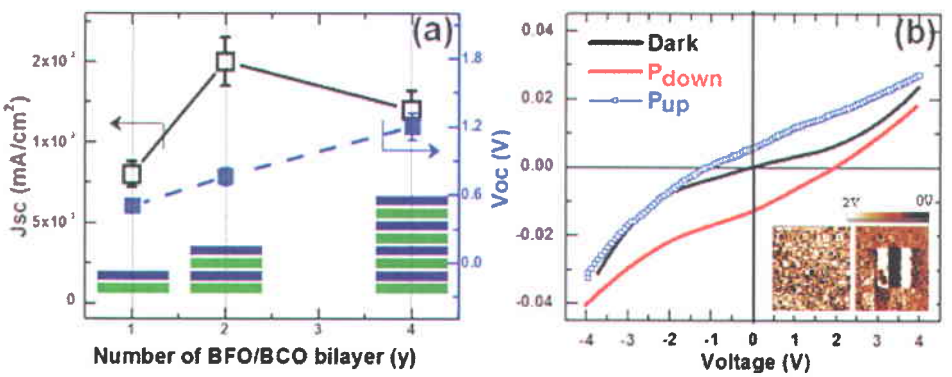

Figure 3.6 (a) Evolution of main PV parameters with number of BFO/BCO bilayers (b) PV properties of the BFO/BCO (15/4) heterostructures after applying pulse bias of ± 15V. The inset shows z-PFM image (5 x 5 μm) with constant applied voltage and variable (± 5V) applied voltage respectively, confirming the switching of ferroelectric polarization.

3.3.5 Calculation of Power Conversion Efficiency

The J-V curve taken at the state of negative and positive poling reveals that the two J_{sc} values (differences between zero crossing of x-y axis and the crossing of J-V curve and y- axis in poled and unpoled state) are not of identical absolute value. This relates to the fact that the total PV effect also contains the electrode-film interface contribution. According to reference [9], we found that the ferroelectric polarization induced internal electric field represents a major contribution (70 %) to the observed PV effect. Power conversion efficiency is calculated by following this formula: Efficiency, $(\eta) = (V_m * J_m)/P_{in}$ where P_{in} indicates the power density of incident solar spectrum in mW/cm^2 and V_m and J_m is shown in **Figure 3.7**. In this work, the values (fill factor and power conversion efficiency) correspond to bulk PV effect only. A maximum power conversion efficiency is obtained from BFO/BCO (15/4) films, of the order of 0.01 % with a fill factor (FF) of about 0.31 [FF= P_{out}^{max} /(V_{oc}*J_{sc})].

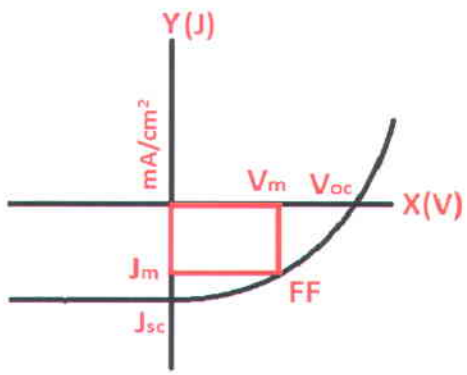

Figure 3.7 Typical J-V curve under illumination

3.4 Result and Discussion

The observed PV phenomena i.e. variation of current density and open circuit voltage in all devices can be described by absorption of solar spectrum as a function of penetration depth. According to Lambert-Beer's Law, the intensity of light is decreased exponentially with the depth in material. The absorption depth is given by the inverse of the absorption coefficient, or α^{-1}. The absorption depth gives the distance into the material at which the light drops to about 36% of its original intensity. Therefore, in PV cell, a particular wavelength of light is required to be

absorbed for a critical thickness without losing intensity. Since the optical direct band gap of BFO (~2.77 eV) [10] and BCO (~2.95 eV) [11] is close to each other, we assume homogeneous bandgap for whole volume of the structure. But thickness of samples depends on the incorporation of number of bilayer. BFO/BCO (15/2) shows higher generation of photocurrent mainly due to higher absorption of spectrum suggesting that a multilayer thickness of 60nm is optimum among all other devices. In the case of BFO/BCO (15/4), first two bilayers contribute toward maximum photocharge carrier generation whereas the photo carrier generation in bottom bilayers decreases. BFO/BCO (15/4) exhibits higher V_{OC} because photogenerated charges trapped at the BFO/BCO interfaces that can build additional electro-potential barriers, which impede slightly the movement of the following charge carriers since the interface is very low. The same reason could explain why photocurrent and photo voltage of BFO/BCO (15/1) is lower than others.

Future studies will investigate the role of the $BiFeO_3$-$BiCrO_3$ interface in the formation of Bi_2FeCrO_6 with an even smaller bandgap and enhanced bulk PV properties. Additional experiments on kinetics vs. thermodynamics during film growth are required to better describe the formation of the interface. Raman scattering and optical absorption measurement are expected to establish the nature and type of interface forms and to address its effect on PV characteristics.

3.5 Conclusion

In summary, we demonstrated the tunability of photocurrent density and photo voltage by tailoring the thickness and number of BFO/BCO bilayers in the overall heterostructure. A maximum PV power conversion efficiency (~0.01%) is observed in samples with the highest number of bilayers. This is mainly due to the linear increase of photovoltage with the stacking number of BFO/BCO bilayer. Thickness dependent absorption coefficient is employed to explain the behavior of observed photocurrent density and photovoltage in all devices. Future work will involve Raman scattering [12, 13] and absorption measurements, to establish and investigate the nature and properties in depth of the interlayer formed at the BFO/BCO interface. Moreover, detailed studies on different growth conditions focusing on the tuning of kinetics and thermodynamics could be an effective way to understand the interfacial phenomena.

3.6 References

[1] R. Nechache, C. Harnagea, S. Licoccia, E. Traversa, A. Ruediger, A. Pignolet, and F. Rosei Appl. Phys. Lett. **98**, 202902 (2011)

[2] S. Y. Yang, L. W. Martin,S. J. Byrnes,T. E. Conry,S. R. Basu,D. Paran, L. Reichertz, J. Ihlefeld, C. Adamo,A. Melville,Y.-H. Chu, C.-H. Yang, J. L. Musfeldt,D. G. Schlom, J. W. Ager and R. Ramesh, Appl. Phys. Lett. **95**, 062909 (2009)

[3] S. Y. Yang, J. Seidel, S. J .Byrnes, P. Shafer, C.-H. Yang, M . D .Rossell, J. F. Scott, J. W. Ager, L.W. Martin, P. Yu, Y.-H. Chu, and R. Ramesh, Nature Nanotech. **5**, 143 (2010)

[4] M. Alexe and D. Hesse, Nature Comm. **2**, 256 (2011)

[5] R. Nechache, P. Gupta, C. Harnagea, and A. Pignolet, Appl. Phys. Lett. **91**, 222908 (2007)

[6] N. Ichikawa et al.,Appl. Phys. Exp. **1**, 101302 (2008).

[7] H. Béa, M. Bibes, S. Fusil, K. Bouzehouane, E. Jacquet, K. Rode, P. Bencok, and A. Barthélémy, Phys. Rev. B **74**, 020101(2006)

[8] M. Qui, K. Yao, Y. C. Liang, J. Appl. Phys. 105, 061624 (2009)

[9] F. Zheng, Jie Xu, L. Fang, M. Shen, and X. Wu, Appl. Phys. Lett. 93, 172101 (2008)

[10] A. Kumar, R. C. Rai, N. J. Podraza, S. Denev, M. Ramirez,Y. Chu, L. W. Martin, J. Ihlefeld, T. Heeg, J. Schubert, D. G. Schlom, J. Orenstein, R. Ramesh, R. W. Collins, J. L. Musfeldt, V. Gopalan, Appl. Phys. Lett. **92**, 121915 (2008)

[11] C. Himcinschi, L. Vrejoiu, T. Weißbach, K. Vijayanandhini, A. Talkenberger, C. Ro¨der, S. Bahmann, D. R. T. Zahn, A. A. Belik, D. Rafaja, J. Kortus, J. of Appl. Phys. 110, 073501 (2011)

[12] J. Andreasson, J. Holmlund, S. G. Singer, C. S. Knee, R. Rauer, B. Schulz, M. Käll, M. Rübhausen, S.-G. Eriksson, L. Börjesson, and A. Lichtenstein, Phys. Rev. B **80**, 075103 (2009).

[13] J. Andreasson, J. Holmlund, R. Rauer, M. Käll, L. Börjesson, C. S. Knee, A. K. Eriksson, Sten-G. Eriksson, M. Rübhausen, and R. P. Chaudhury, Phys. Rev. B **78**, 235103 (2008).

Chapter 4 Photovoltaic Effect in Multiphase Bi-Mn-O Thin Films

4.1 Introduction

In photovoltaic devices, photons with energy higher than the band gap of the material are absorbed to produce electron-hole pairs, which are separated by an internal electric field and collected by the electrodes. Effective photo carrier separation depends on internal electric field set up inside material. Basically it comes from p-n homo or hetero-junction [1] that forms depending on the semiconductor types in solar cell. To collect the photo carrier effectively in this case, electrodes are required to connect semiconductor ohmically. On the other hand, semiconductor-electrodes interface creates schottky barrier [1] that also could separate photo generated carrier. However, ferroelectric material which possesses polarization induced internal electric field called depolarization field (E_{DP}) extended over the whole thin film volume [2,3] splits up photo charge carrier efficiently. Unlike a p-n junction or metal-insulator junction interface where depletion region takes part in photo carrier separation, depolarization electric field of ferroelectric material drives the photo carrier towards electrodes. Therefore, a combined effect of electrical properties of normal *p-n* junctions, semiconductor-metal interface and the exotic properties of ferroelectric oxides have been the subject of intensive theoretical and experimental studies in photovoltaic research.[4,5,6] The photovoltaic properties of numerous ferroelectric oxides have been investigated such as $BaTiO_3$ (BTO) and $Pb(Zr,Ti)O_3$ (PZT). [7,8,9] Relatively large band gap of those ferroelectric materials hinder of getting high power conversion efficiency (typically in the order of 10^{-7}-10^{-5}).

The low bandgap of MF materials (typically ranging from 1.1 eV to 2.7 eV) is an essential key parameter in terms of green energy research since about 93% of solar radiation is concentrated in the visible and infrared light with wavelength (l) in the range of 0.31–3.18 eV).[10] The most widely investigated MF materials for such applications are $BiFeO_3$ (BFO) [11] and Bi_2FeCrO_6 (BFCO) [12]. $BiMnO_3$ (BMO) is the most "fundamental" one, as it is referred to as the "hydrogen atom" of multiferroic materials.[13] Among known MFs, BMO exhibits the lowest

bandgap (typically 1.2 eV) and a ferroelectric polarization of up to 16 $\mu C/cm^2$ in thin film form.[14] The crystal structure of BMO films belongs to the monoclinic C2 space group with lattice parameters as follows: a =9.523 Å, b =5.6064 Å, and c = 9.8536 Å, $\alpha = \gamma = 90°$, and β =110.667°, at room temperature. The low band gap of ferroelectric BMO films results in higher light absorption and reduced photo charge recombination, a critical issue to be addressed for improving the PV efficiency in this system. The high leakage currents usually observed in these films make ferroelectric measurements quite challenging because of induced strain in the film arising from lattice mismatch. The resistivity of the film directly related with leakage current depends not only on the optimized growth condition of films [15,16] but also the device structure to reduce the leakage current.[12] The growth conditions, crystal structure and quality of the as prepared BMO films are the most fundamental parameters for tuning functional properties.

Here, we describe the pulsed lased deposition (PLD) growth of Bi-Mn-O thin films on (111)-oriented $SrTiO_3$:Nb (STO:Nb) substrate. The Bi/Mn ratio was varied to study the physical properties of obtained films. Films crystallize in two phases, Mn_3O_4 and BMO, both epitaxially grown on STO substrate. The electrical and optical characterizations highlight the Bi/Mn ratio dependent PV effect in such system. The results demonstrate that increased percentage of BMO phase in the films contributes more to enhance PV efficiency.

4.2 Growth condition and effect of PLD growth parameters

The 70 nm-thick films were grown directly on (111) oriented STO:Nb substrates by PLD using stoichiometric composition of BMO target. According to the chemical formula of BMO appropriate amounts of Bi_2O_3 and Mn_2O_3 oxides were ball-milled, dried and sintered to synthesize the PLD target. Laser fluence and pulse frequency were ~ 2.0 J /cm^2 and 4 Hz, respectively. Before deposition, the deposition chamber was pumped to a vacuum level of 1 x 10^{-5} mbar. The substrate temperature and the oxygen pressure during growth were varied in the ranges of 25–40 mTorr and 595–670 °C, respectively. Table 1 shows the energy dispersive spectrometry (EDX) results carried out in scanning electron microscopy (SEM) on Bi-Mn-O films together with deposition conditions and observed phases in the films. The bismuth versus manganese (Bi/Mn) atomic ratio is clearly sensitive to deposition temperature and oxygen

pressure mainly due to the high volatility of Bi element. Table 4-1 illustrates also the energy threshold extracted from the optical measurements.

Table 4-1 Phases, compositions and optical properties of Bi-Mn-O films grown on (111)-oriented $SrTiO_3$ substrates

Film #	Deposition temperature (^{0}C) & pressure (mTorr)	Bi/Mn ratio (at. %)	phases	Energy threshold (eV)
A	595, 25	0.82	$BiMnO_3/Mn_3O_4$	1.2
B	670 , 40	0.56	$BiMnO_3/Mn_3O_4$	1.5/2.2
C	670 , 25	0.14	$BiMnO_3/Mn_3O_4$	2.6

Near-stoichiometric composition can only be achieved by growing at low temperature (**Film A- 595 °C**) whereas a higher deposition temperature (e.g. 670 ^{0}C) yields manganese-rich films (**Film C**). Increasing the flow of oxygen at higher deposition temperature (from 25 to 40 mTorr) minimizes Mn or increases Bi in the film (**Film B**). Bi deficiency is due to its evaporation at high temperature, since this element is highly volatile. These results are consistent with several previous reports on other Bi-based perovskite systems.[17,18]

4.3 Structure and Morphology

4.3.1 XRD Analysis: θ-2θ and Φ scan measurement

Figure 4.1 (a) shows x-ray diffraction spectra of the obtained films which evidence their bi-phase character. The θ-2θ scans (**Figure 4.1**a) reveal the preferential monoclinic (11-1)m orientation of BMO phase following the cubic $(111)_c$ direction of $SrTiO_3$ substrate. They also indicate the presence of additional phase, identified as Mn_3O_4 phase in all prepared films. This phase exhibits a preferential orientation along the tetragonal $(101)_t$ direction. Phi (Φ) scan measurements around STO (110) reflection indicates epitaxial growth of BMO and Mn oxide phase on STO:Nb substrates with threefold symmetry (**Figure 4.1**b). The orientation relationships are as following: $BiMnO_3$ (110)pc//$SrTiO_3$ (110)c//Mn_3O_4 (110)pc. The similar multiphase epitaxial growth is previously reported in reference [19].

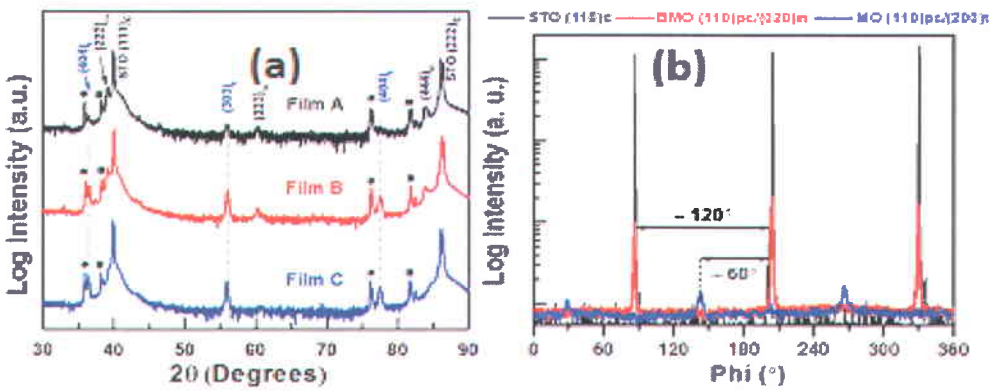

Figure 4.1 (a) XRD θ-2θ scans of Film A, Film B and Film C grown on (111) oriented Nb: STO substrate shows reflections of $(11\text{-}1)_m$ orientation of BMO and $(101)_t$ orientation of Mn_3O_4 phases. Circular and rectangular symbols in (a) indicate (00l) K_β lines and tungsten contamination of x-ray tube source. (b) Φ scan measurements show the three fold symmetry of BMO and Mn oxide phases in the films.

4.4 Photovoltaic effect: current-voltage (I-V) measurement

To perform electrical measurements, 2D arrays of Indium Tin Oxide (ITO) top electrodes were deposited by PLD through a shadow mask, at 200 °C under 10 mTorr oxygen partial pressure. Electrical measurements were performed by applying a bias voltage between the ITO top electrodes and the niobium doped STO substrate, which acts as a bottom electrode.

Figure 4.2 illustrates the obtained current density-voltage (J-V) curves taken under both dark and 1.5 AM sun illumination (100 mW/cm^2). **Figure 4.2 (a) & (b)** (J-V plotting of olive green color) displays the dark current and PV effect of the as-grown Film A. The samples were subsequently electrically poled by applying a microsecond voltage pulse of ±10 V between top and bottom electrodes. This method supposed to allow the switching of ferroelectric polarization up or down along the normal direction.[20] Only Film A & B exhibit a PV effect (Data from Film C is not shown as it is not significant in terms of efficiency measurements).

Figure 4.2 (b) & (d) shows the switching of the current-voltage (J-V) curve obtained after applying alternating voltage pulses, inducing the reversal of the direction of polarization in the films. The dark current measurements reported in **Figure 4.2 (d)** were taken after downward

poling. Film A gives V_{oc} of ~0.56 V and J_{sc}~0.23 mA/cm^2, whereas lower values, 0.22 V and 0.11 mA/cm^2 were recorded for Film B. The calculated maximum PCEs in Film A and B are 0.1% and 0.01%, respectively. Likewise, the fill factor (FF) of Film A is higher (~0.71) than the one of Film B (~0.47) [FF= P_{out}^{max} /(V_{oc}*J_{sc})]. These results demonstrate that the film with higher Bi/Mn ratio generates high power conversion efficiency.

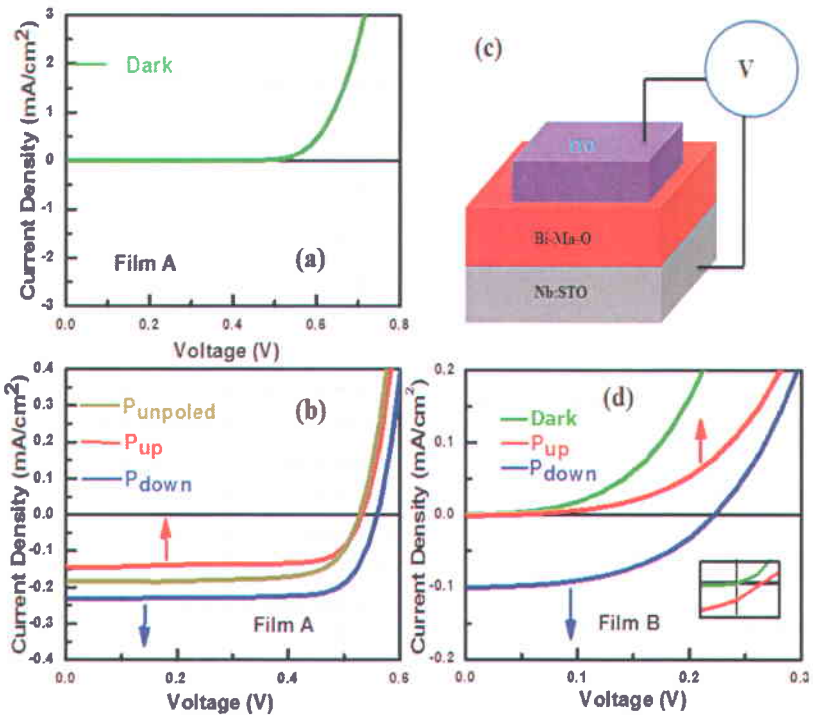

Figure 4.2 (color on line) J-V characteristic curves of Film A (a) and (b) Film B (d) respectively, with positive and negative poling demonstrating the photovoltaic (PV) effect. The inset in (d) represents a zoom of the J-V curve around origin. The geometry of the tested structure is illustrated in (c).

4.5 Ferroelectricity measurement: PFM study

Figure 4.3 shows the macroscopic polarization of Film A & B (without illumination) as a function of applied voltage. We found a remnant polarization of 6.6 μC/cm^2 for the film A and 5.5 μC/cm^2 for film B, values far below the reported one for the BMO film in Ref. **[14]**.

The loops are well-saturated at negative bias (polarization up) and show a significant leakage contribution on the positive side, consistent with the J-V curves in Fig. 4.2.

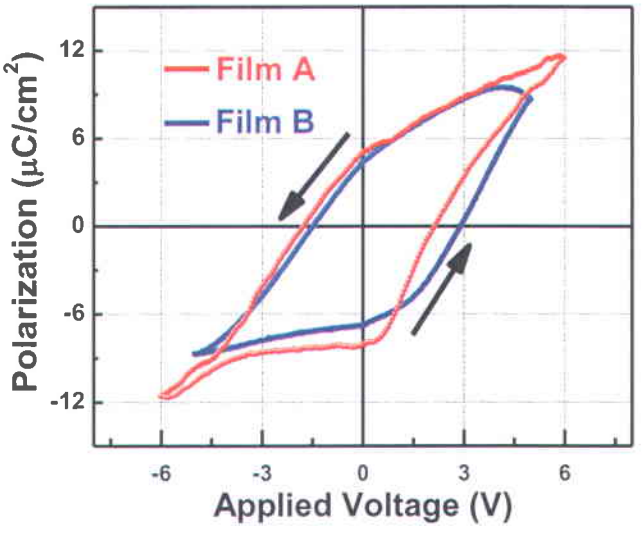

Figure 4.3 Voltage vs Polarization curve of Film A & B

The hysteresis loop of Film B shows a more pronounced leaky character, probably due to a larger density of interphase boundaries that imply a higher density of defects, but the existence of a switchable ferroelectric polarization is indubitable, as proven by measurements at different cycling frequencies, as shown in Fig. 4.4.[21] The fact that the hysteresis loop parameters do not change significantly when modifying the cycling frequency by a factor of 20 prove that the measured charge flow originates in the switching of polarization and is not due to other effects.[22,23]

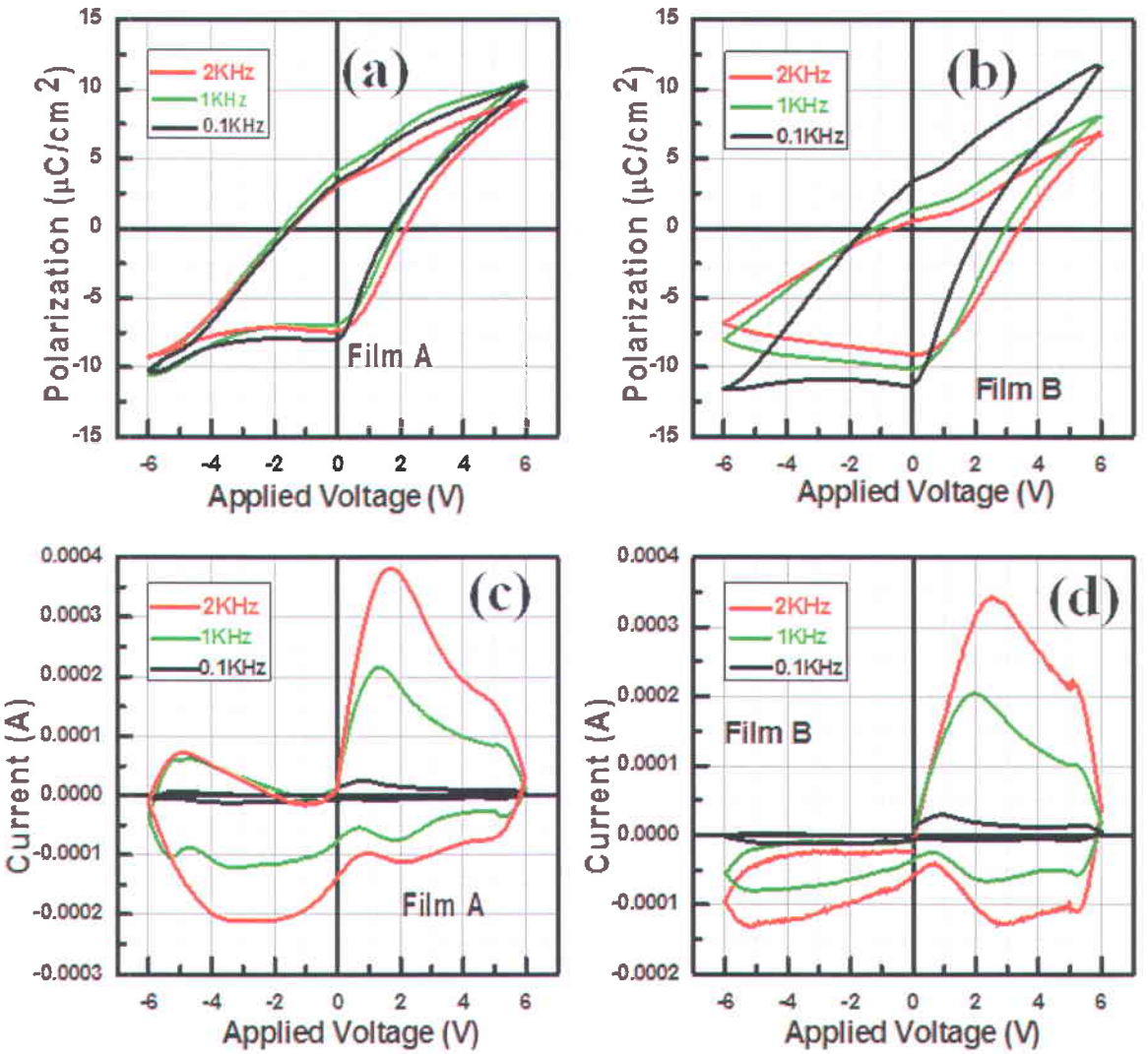

Figure 4.4 Ferroelectric hysteresis loops (a, b) and the corresponding current loops (c,d) at different cycling frequencies: while there is a significant leakage contribution, the fact that the switching current dominates at low frequency proves the existence of the ferroelectric component.

Beside the leakage, another important property that can be extracted from the ferroelectric loops is the imprint of polarization. As can be seen in **Fig 4.3**, the positive coercive voltage is higher than the negative one, and the fact that polarization requires a higher voltage to switch downward implies that there is an internal built-in field opposing this process. This net field

oriented upward has a major contribution to the charge separation, as we shall discuss below. At the same time, in the film/STO interface region polarization is pinned downwards most likely due to the internal stresses caused by the lattice mismatch. This imprint of polarization was confirmed by piezoresponse force microscopy, shown in Fig. 4.5.

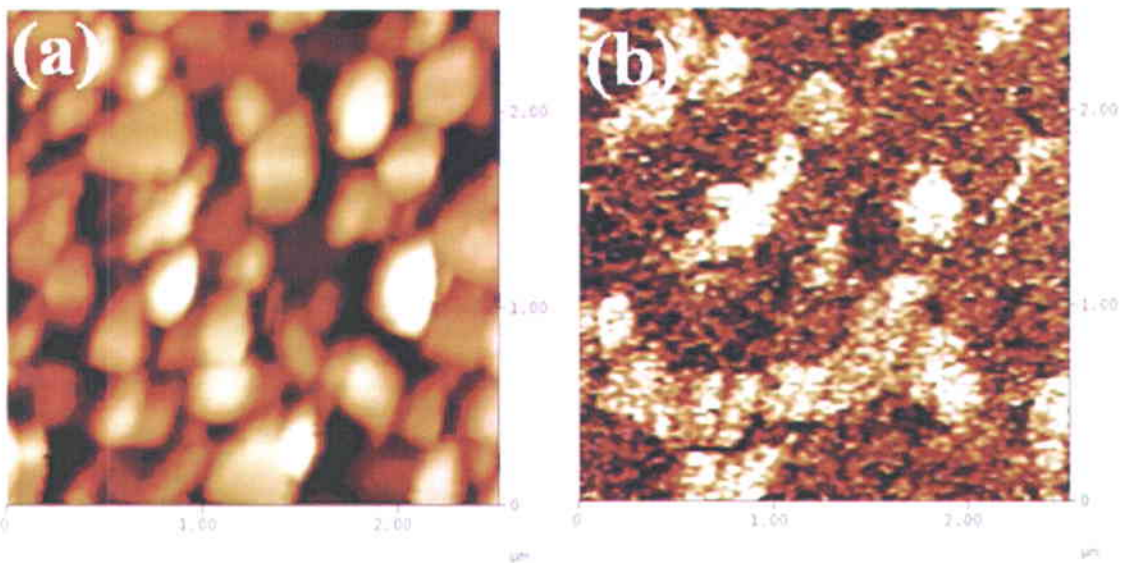

Figure 4.5 piezoresponse force microscopy measurement showing that the as-grown epitaxial BMO/Nb:STO(111) heterostructure has the polarization oriented downward (bright contrast). (a) surface topography, and (b) PFM image. The regions/grains that do not show a response are either oriented in-plane, or represent the minor MO phase.

4.6 X-ray photo spectroscopy (XPS) analysis

The electronic and chemical properties of Film A were analyzed by X-ray photoelectron spectroscopy (XPS). Figure 4.6 exhibits the Mn $2p_{3/2}$ peak spectrum of Film A. The peak is deconvoluted into corresponding peak of Mn^{2+}, Mn^{3+} and Mn^{4+} valence states with the binding energy of 641 eV, 641.66 eV and 642.75 eV respectively.[24,25] Comparing the area under each curve, it can be concluded that Mn^{3+} state is the highest valence state in this film.

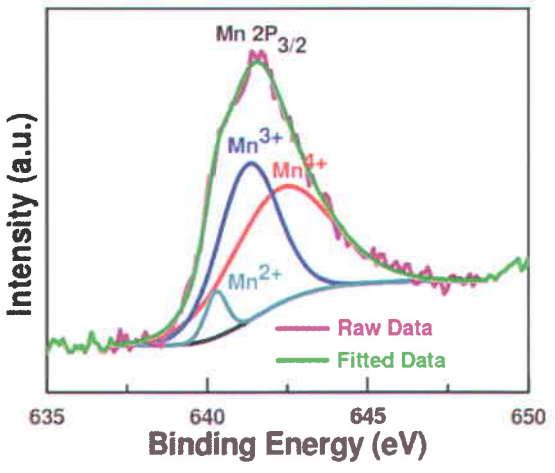

Figure 4.6 Deconvoluted XPS spectra of the Mn $2p_{3/2}$ peak

4.7 Optical Absorption: Spectroscopic Ellipsometry Measurement

To investigate the absorption properties of epitaxial films, room temperature VASE measurements were performed in the 1.25 eV up to 3.35 eV range at five angles of incidence (i.e. 55, 60, 65,70 and 75°) using a VASE ellipsometer from J.A. Woollam Company. The absorption coefficients $\alpha = 4\pi k/\lambda$ (where k and λ denote the extinction coefficient and wavelength, respectively) estimated for the different films are presented as a function of photon energy $E <$ 3.5 eV in **Figure 4.7** a.

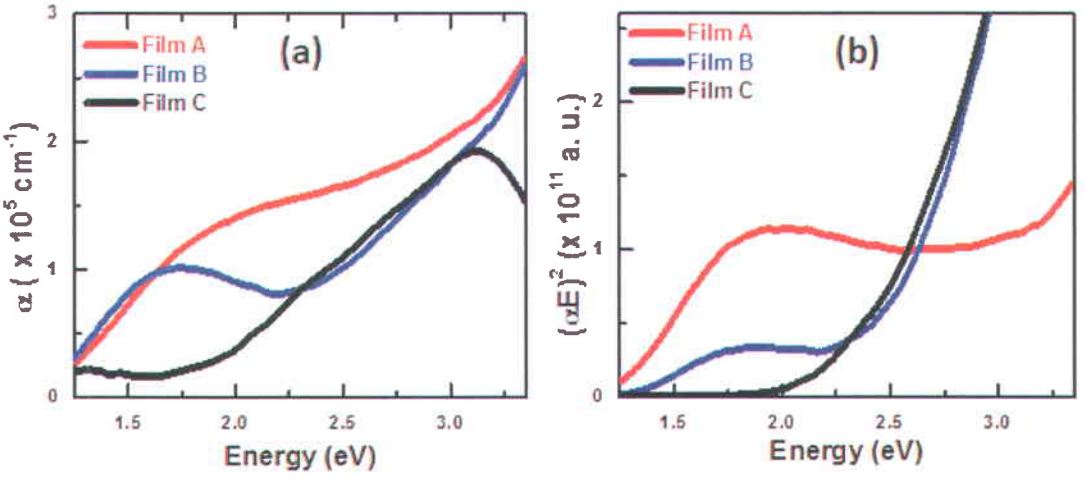

Figure 4.7 (a) Optical absorption coefficient (α) curves as a function of photon energy, measured by Ellipsometry for multiphase Bi-Mn-O thin films. (b) corresponding estimated direct bandgaps.

By increasing the BMO phase in the films, the 2.0 eV charge gap (Film C) broadens and begins to redshift and eventually develops into the 1.6 eV band in Film A (cf. Fig. 4.7 b). Plots of $(\alpha E)^2$ versus photon energy place the band gap in Film A and Film C at ~1.1 and 2.3 eV, respectively (cf. Fig. 4.7 b). These values are close to those previously observed in BMO films[26] and well document Mn_3O_4.[27, 28] In the BMO case, comparing with theoretical and experimental spectra of chemically similar materials, like $LaMnO_3$,[29,30] where Mn^{3+} centers are in locally distorted octahedra at the near infrared band of 1.6-1.9 eV (with an overall intensity α around 10^5 cm^{-1}), is assigned to complex combination between O 2*p* and Mn 3*d* states (p-d) charge transfer excitations and inter-site $d(e_g)$-$d(e_g)$ high spin charge transfer (HS CT) transitions.[31] The particular shape of $(\alpha E)^2$ plot obtained for Film B, where two linear parts (i.e. 1.1 and 2.2 eV) are distinguished, clearly indicates that the optical properties of our BMO thin films are a superposition of spectral responses of BMO and Mn oxide.

4.8 Result and Discussion

The non-zero photovoltage and photocurrent observed in Film A (unpoled state) can be described in terms of the interfacial effect i.e. interface PV phenomena [32,33]. In this model, we neglect ferroelectric effect in the unpoled films. Also we neglect Mn oxide phase in the film for photovoltaic effect analysis because of the presence of higher percentage (~ 85 % with ~2% error) of $BiMnO_3$ phase in the Film A. The percentage of two phases has been mathematically calculated by taking into account Bi/Mn atomic ratio measured in EDS-SEM. Neglecting the MO phase is justified by the fact that Film C, which contains a higher amount of the MO phase, does not harvest any significant electricity. We then performed Ultra-violet photoemission spectroscopy (UPS) measurements on the BMO films in order to determine the position of the valence band energy (E_V) and Fermi energy (E_F). Taking into account the band gap of BMO phase (~1.1 eV), we calculated electron affinity of Film A from the following equation: $\chi = h\gamma - W - E_g$ where 'W' and 'hγ' (21.2 eV) denotes the width of the photoemission spectrum and excitation energy respectively. The calculated electron affinity is ~3.03 eV ± 0.2. The resulting

band diagram of the ITO/BMO/STO heterostructure before and after its formation is shown in **Figure 4.8**. Electron affinity and band gap of doped STO has been obtained from reference [34]. In this diagram we assumed an ideal interface where the traps at the film/Nb:STO interface are neglected [1]. **Figure 4.8** (a) shows the position of the E_F slightly below the middle of the band gap which implies the film has a p-type conduction, probably caused by a low amount of Bi vacancies, as is often the case for Bi-based perovskites thin films due to the high volatility of Bi element. Nonetheless, many reports described that niobium doped STO is able to generate photoexcitons under illumination and acts as a n-type material.[35,36,37] Thus, in our heterostructure, the net effect of the formation of both a p-n junction and a Schottky junction at the interface of film/substrate and film/top electrode, is an electric field oriented upward, which separates the photo generated charge carriers. The theoretically calculated net internal potential is $\Delta\Phi_{B\_ITO/BMO/Nb:STO} = 0.62$ eV. The actual photovoltage is a little bit lower because of surface states at the interfaces that reflect in our experimentally yielded photovoltgae (V_{OC}) in the unpoled state. **Figure 4.8** (b) illustrates the possible charge flow in film/substrate junction under illumination. The band bending at film/STO interface that shown here is assumed to be very similar to TiO2/Si contact in a photo electrochemical cell.[38] The e^-/h^+ pairs are generated in both film and STO. Under illumination, electron transfer starts to set up in the junction due to the difference of quasi Fermi energy level of electron and holes. The photogenerated electrons in the film are swept away towards the ITO/film interface due to the internal built-in field established at film/substrate junction. Photo generated holes recombine with a fraction of electrons in the conduction band of STO. This recombination at the junction reduces the loss of holes in the STO thus increasing the photocurrent. A portion of generated photoelectrons in STO also might transfer into conduction band of film. However, **Figure 4.8** (c) shows the overall band bending, where the Schottky field is higher and oppositely directed with respect to the field set up at the BMO/STO interface. Therefore, the net electron flow will be from top to the bottom electrode due to the effect of the net electric field, in good agreement with the J-V curve and with the imprint of polarization inferred from the hysteresis loops. The whole mechanism has been illustrated schematically in **Fig. 4.8** c.

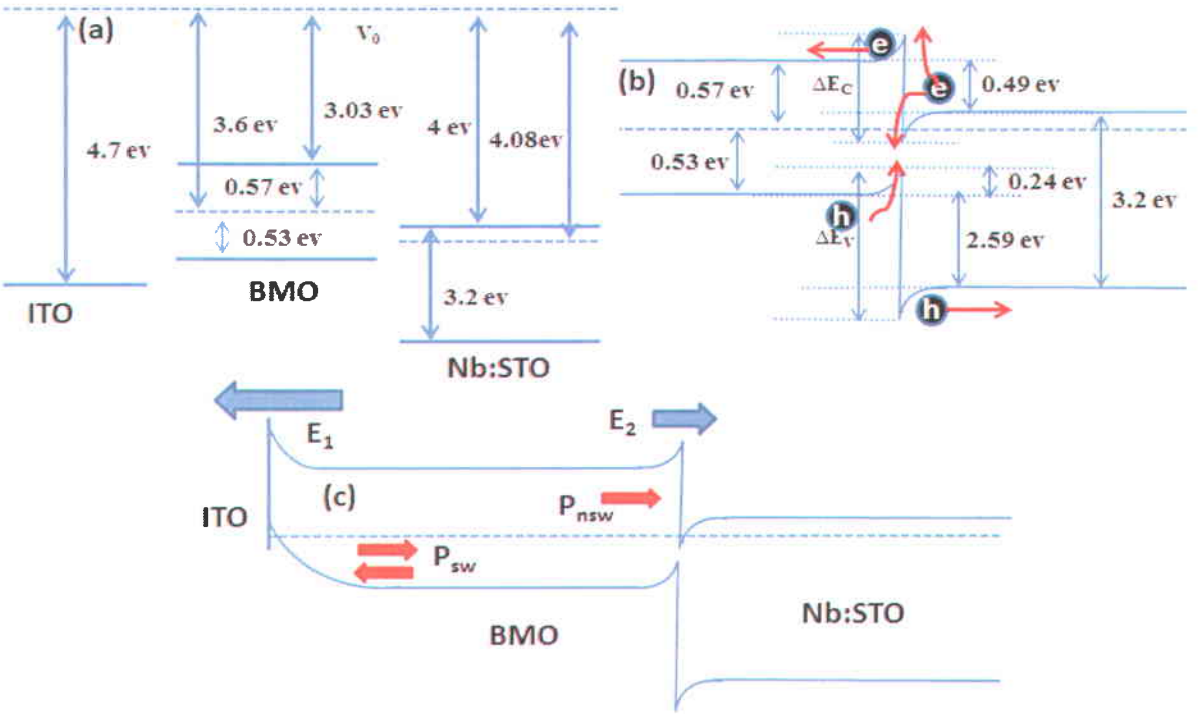

Figure 4.8 (a) Energy band diagram of isolated ITO, BMO and doped STO (b) Energy band diagram of an ideal BMO/Nb:STO interface at thermal equilibrium (c) Energy band diagram of ITO/BMO/Nb:STO interface with showing the polarization effect.

Taking into consideration the ferroelectric polarization, it is possible to explain the tunability of the J-V curve. Depending on the direction of the switchable ferroelectric polarization, aggregated bound charges (+ve or -ve) at the interface of the p-n junction might penetrate (decrease or increase) the depletion width and height of potential barrier, an effect called polarization modulation effect.[39,40] This modulation effect can explain the tunability of the J-V curve in **Fig. 4.2**. As shown in **Fig. 4.8 c**, there are two parts of ferroelectric polarization: non switchable polarization (P_{nsw}), originates from the compressive strain in the film (polarization pinning at the film/electrode interface), and switchable polarization (P_{sw}). Elaborately, the depolarization field associated with the polarization oriented towards the bottom electrode reduces the width of the film/STO interface resulting in a small increase and decreases the barrier height of film/STO and film/ITO simultaneously. Therefore, current flow will be higher in this case, as shown in **Fig. 4.2**. The opposite direction of polarization modulates the barrier width and height of film/electrodes in a similar fashion, which results in a small reduction

of the current density compared to the unpoled condition. However, estimation of electric field at each interface and the estimation of polarization induced electric field could give the contribution of each on observed photocurrent and photovoltage. Investigating each individual contribution could help to elucidate which one dominates the current flow, and this is the subject of a future investigation.

4.9 Conclusion

We report the photovoltaic properties of epitaxial BMO-MO films on (111)-oriented Niobium doped STO substrates. We found an external power conversion efficiency of ~0.1% in the films when illuminated under sun simulator (AM 1.5G). Our results show that the photocurrent and photo voltage strongly depend on the Bi/Mn ratio in the film, with the best power conversion efficiency being obtained in films with a high ratio of Bi/Mn and thus a high BMO content. A traditional p-n junction based interfacial model has been employed to explain the photovoltaic effect that is significantly affected by the spontaneous polarization.

4.10 References

[1] S. M. Sze, Semiconductor Devices: Physics and Technology, 2nd ed. (Wiley, New York), Vol. 4, pp. 124–127 (2002)

[2] F. Zheng, J. Xu, L. Fang, M. R. Shen, Z. L. Wu, Appl. Phys. Lett. 93, 172101, (2008).

[3] W. Ji, K. Yao, Y. C. Liang, Adv. Mater. 22, 1763 (2010).

[4] Z. Luo, J. H. Hao, J. Gao, Appl. Phys. Lett. **91**, 062105 (2007).

[5] Y. S. Xiao, X. P. Zhang, and Y. G. Zhao, Appl. Phys. Lett. **90**, 013509 (2007)

[6] S. M. Guo, Y. G. Zhao, C. M. Xiong, P. L. Lang, Appl. Phys. Lett. **89**, 223506 (2006).

[7] M. Glass, D Von der Linde and T. J. Negran, *Appl. Phys.Lett.* **25** 233 (1974)

[8] Y. S. Yang , S. L. Lee, S. Yi, B. G. Chae, S. H. Lee, H. J. Joo, M. S. Jang, *Appl. Phys. Lett.* **76** 774 (2000)

[9] L. Pintilie, I. Vrejoiu, G. L. Rhun, M. Alexe, *J. Appl.Phys.* **101** 064109 (2007)

[10] H. R. Condit, F. Grum, Spectral Energy Distribution of Daylight. J. Opt. Soc. Am. **54**, 937 (1964).

[11] Y. Chu, Q. He, C. Yang, P. Yu, L. W. Martin, P. Shafer, R. Ramesh, Nano lett. **9**, 1726-1730 (2009)

[12] R. Nechache, C. Harnagea, A. Pignolet, F. Normandin, T. Veres, L. Carignan, D. Ménard, Appl. Phys. Lett. **89**, 102902 (2006).

[13] N. A. Hill, K. M. Rabe, Phys. Rev. B **59**, 8759 (1999).

[14] J. Y. Son, Y. H. Shin, Appl. Phys. Lett. 93, 062902 (2008)

[15] W. Eerenstein, F.D. Morrison, J.F. Scott, and N.D. Mathur, Appl. Phys. Lett. **87**, 101906 (2005).

[16] H. Chiba, T. Atou, Y. Syono, J. Solid State Chem. **132**, 139, 1997.

[17] H. Béa, M. Bibes, S. Fusil, K. Bouzehouane, E. Jacquet, K. Rode, P. Bencok, A. Barthélémy, Phys. Rev. B **74**, 020101 (2006).

[18] R. Nechache, C. Harnagea, L.-P. Carignan, O. Gautreau, L. Pintilie, M. P. Singh, D. Menard, P. Fournier, M. Alexe, A. Pignolet, J. Appl. Phys. **105**, 061621 (2009).

[19] S. Fujino, M. Murakami, S. H. Lim, L. G. Salamanca-Riba, M. Wuttig, and I. Takeuchi, Journal of Applied Physics 101, 013903, 2007

[20] A. Sharan, J. Lettieri, Y. Jia, W. Tian, X. Pan, D. G. Schlom, V. Gopalan, Physical Review B **69**, 214109, 2004

[21] H. Jeen, G.S-Bhalla, P.R. Mickel, K. Voigt, C. Morien, J. Appl. Phys. **109**, 074104 (2011).

[22] J. F. Scott, J. Phys: Condens Matter. 20, 21001 (2008)

[23] L. Pintilie and M. Alexe, Appl. Phys. Lett. 87, 112903 (2005)

[24] J. Wei, D. Xue, C. Wu, Z. Li, J. of Alloys and Compounds. 453, 20 (2008).

[25] C. F. Chung, J. P. Lin, J. M. Wu. Appl. Phys. Lett. 88, 242909 (2006).

[26] X.S. Xu, J.F. Ihlefeld, J.H. Lee, O.K. Ezekoye, E. Vlahos, R. Ramesh, V. Gopalan, X.Q. Pan, D. G. Schlom, J. L. Musfeldt, Appl. Phys. Lett. **96**, 192901 (2010).

[27] D.P. Dubal, D.S. Dhawale, R.R. Salunkhe, S.M. Pawar, V.J. Fulari, C.D. Lokhande, J. Alloys Compd. **484**, 218 (2009).

[28] H.Y. Xu, S.L. Xu, X.D. Li, H. Wang, H. Yan, Appl. Surf. Sci. **252**, 4091 (2006).

[29] M.A. Quijada, J.R. Simpson, L. Vasiliu-Doloc, J.W. Lynn, H.D. Drew, Y.M. Mukovskii, S.G. Karabashev, Phys. Rev. B **64**, 224426 (2001).

[30] N.N. Kovaleva, A.V. Boris, C. Bernhard, A. Kulakov, A. Pimenov, A.M. Balbashov, G. Khaliullin, B. Keimer, Phys. Rev. Lett. **93**, 147204 (2004).

[31] A.S. Moskvin, A.A. Makhnev, L.V. Nomerovannaya, N.N. Loshkareva, A.M. Balbashov, Physical Review B **82**, 035106, 2010

[32] M. Qin, K. Yao, Y.C. Liang, B.K. Gan, Appl. Phys. Lett. **91**, 1 (2007)

[33] A. Matsumura, Y. Kamaike, T. Horiuchi, M. Shimuzi, T. Shiosaki, K. Matsushige, Japanese J. Appl. Phys., **34**, 5258 (1995).

[34] H. Yang, H. M. Luo, H. Wang, I. O. Usov, N. A. Suvorova, M. Jain, D. M. Feldmann, P. C. Dowden, R. F. DePaula, Q. X. Jia, Appl. Phys. Lett. 92, 102113, (2008)

[35] Z. Yue, K. Zhao, S. Zhao, Z. Lu, X. Li, H. Ni, A. Wang, *J. Phys. D: Appl. Phys.* 43, 015104 (2010)

[36] T. Muramatsu, Y. Muraoka, Z. Hiroi, arXiv:cond-mat/0404372, (2004)

[37] F. Horikiri, T. Ichikawa, A. Kaimai, H. Matsumoto, K. Yashiro, T. Kawada, J. Mizusaki, http://www.electrochem.org/dl/ma/206/pdfs/1783.pdf

[38] Y. J. Hwang, A. Boukai, P. Yang, Nano Lett. 9, 410 (2009)

[39] Y. Watanabe, Phys. Rev. B 59(17), 11257 (1999)

[40] R. Meyer and R. Waser, J. Appl. Phys. 100(5), 051611 (2006).

Chapter 5 Conclusion and Future Perspectives

We conclude that multiferroic materials are viable candidates for use as active elements in photovoltaic devices, due to the coexistence of ferroelectricity and magnetism in the same phase. Ferroelectricity enables the generation of a polarization-induced electric field inside the material that separates the photogenerated charge carriers efficiently. Nonetheless, magnetic properties of the material induce a lower bandgap, which is one of the key parameters to harness electrical power from sunlight. Despite of showing an excellent mechanism of photo carrier separation, the overall external electrical power conversion efficiency in such type of materials is very poor. The physics behind the photovoltaic effect in multiferroics is still not clearly elucidated, a lot more investigation is still needed to make it clear, while simultaneously looking for an effective way to improve the efficiency. In this work, we succeeded to improve the electrical power conversion efficiency by engineering the material in our first work, showed in chapter 3. We successfully grew several epitaxial BFO/BCO bilayers on CRO coated LAO single crystalline substrates by PLD, employing a compressive strain in the films due to lattice mismatch. We represented the effect of number of incorporated BFO/BCO bilayer and thickness of each layer of the heterostructure to photo generated voltage and current respectively. We also reported the ferroelectric switching of current-voltage (I-V) curve which proved that photovoltaic effect originated from ferroelectric polarization. Our investigations showed that the heterostructure exhibits higher power conversion efficiency than single layer BFO on LAO substrate. Since the optical band gap of BFO and BCO is close to each other, we assume same band gap in the whole structure. Absorption of solar spectrum with varying thickness of the samples explains the behavior and nature of experimentally observed photo voltage and photo current. However, interface of BFO and BCO that formed due to intermixing could play a role on photovoltage and photocurrent, only if any active phase is formed at the interface. But there is no clear evidence on such type of phase formation. Raman scattering and absorption measurement could be an effective tool to know about the nature of interface. Alternatively by varying thickness of each layer and keeping overall thickness constant in all samples could give an idea whether any effect comes from interface or not, that could be a future investigation in details.

In chapter 4, we reported the photovoltaic effect for first time in Bi-Mn-O thin films, grown on (111) oriented niobium-doped STO substrate, by PLD. The films contain an epitaxial BMO compound and Mn oxide phase. Our investigations showed that the BMO compound responded under sun light by exhibiting the PV effect. We obtained higher power conversion efficiency from the film with a higher Bi/Mn ratio. A model of p-n junction is employed to explain our experimental result. Our explanation reports that the PV effect comes from the combined effect of top electrode-film interface, film-bottom electrode interface and ferroelectric polarization. However, it would be very interesting in future to calculate the electric field of each interface together with ferroelectric polarization induced electric field thus percentage contribution of each on PV effect.

Résumé en Français

1. Résumé

La découverte de l'effet photovoltaïque dit « massif » dans les matériaux multiferroiques (MFs) a ouvert de nouvelles perspectives dans le domaine de photovoltaïque (PV). Ceci est dû aux propriétés électriques uniques des MFs qui génèrent des champs électriques non confinés. En effet, la séparation de photocharges générées lors d'une illumination des MFs est liée aux champs électriques induits par la polarisation ferroélectrique spontanée, présente dans ces matériaux à symétrie non-centrosymétrique. De plus, cette polarisation est d'autant plus forte quand les dimensions de ces matériaux sont réduites à l'échelle nanométrique. Par conséquent, l'utilisation de ces matériaux permet l'élimination du besoin de jonctions p-n fréquemment introduites dans les cellules PVs à semi-conducteurs conventionnels. Cependant, l'efficacité de conversion des dispositifs à base des MFs est très faible et à ce jour reste incomparables avec les cellules PV conventionnelles. Ceci est dû principalement aux faibles conductivités électriques et aux larges gaps optiques des MFs puisque ces derniers sont des ferroélectriques, isolants par nature. Le défi ultime pour le développement de dispositifs efficaces et compétitifs exploitant l'effet PV « massif » réside donc dans l'augmentation de la conductivité sans altérer la polarisation ferroélectrique de ce type de matériaux. D'autre part, les gaps des MFs sont généralement aux alentours de 1.2-2.7 eV, un paramètre important pour les mécanismes de génération et de séparation des porteurs de charges, sont faibles comparés à ceux des ferroélectriques, typiquement de l'ordre de ~3-4 eV. Ces faibles gaps permettront une meilleure absorption du spectre solaire et la réduction du taux de recombinaison des porteurs de charges.

Dans ce contexte, mon projet de maitrise portera sur le développement de nouveaux matériaux MFs en couches minces ou en heterostructure et leur intégration dans des dispositifs PV fonctionnels.

Dans la première partie de ce travail, nous avons développé des structures hétéroépitaxiées à base de bicouche de $BiFeO_3/BiCrO_3$ (BFO/BCO) déposées par ablation laser pulsé (PLD). Des substrats $LaAlO_3$ (LAO) orientés (100) recouvert de couche mince de $CaRuO_3$ (CRO) conductrice servant de d'électrode de bas. Un réseau d'électrodes transparentes à base

d'ITO est déposé sur l'hétérostructure pour réaliser les mesures électriques et PV. L'utilisation de cette hétérostructure comme couche PV active exhibe une efficacité de conversion de 0.1% sous illumination équivalente à 1 soleil (AM. 1.5 AM). Le facteur de forme (FF) estimé est de l'ordre de 31%, une valeur probante pour des dispositifs à base d'oxydes ferroélectriques ou de MFs. Nous résultats mettent en exergue le contrôle de photo-courant et la photo-tension générés au moyen de l'épaisseur et le nombre des bicouches BFO/BCO incorporées dans le dispositif. Ceci ouvre de nouvelles perspectives pour la conception d'hétérostructures MFs avec des propriétés PV améliorées et ajustables.

Dans la seconde partie de l'étude, nous avons concentré nos efforts sur l'investigation de l'effet PV « massif » dans le system Bi-Mn-O. Des films minces à base de ce matériau ont été préparés par PLD sur des substrats conducteurs de $SrTiO_3$ dopés au Niobium et orientés (100). Des études structurales détaillées au moyen de la diffraction aux rayons X ont démonté l'existence de deux phases, la perovskite $BiMnO_3$ (BMO) avec une orientation monoclinique $(111)_m$ et celle de Mn3O4 ayant une orientation suivant la direction tétragonale (101)t. Comme révélé par les mesures en balayage phi, les structures deux phases sont reliées epitaxialement a celle du substrat STO. Les mesures des propriétés PV sous une illumination 1 soleil ont démonté l'effet de rapport élémentaire Bi/Mn sur les valeurs du photo-courant et la photo-tension générés dans les dispositifs à base de BMO. Un rendement PV maximal de 0.1% est obtenu quand le rapport Bi/Mn est de l'ordre de 0.82. Cette étude a mis en exergue la complexité des différents mécanismes régissant les propriétés PV du BMO ainsi que les propriétés électriques aux interfaces film-électrodes.

2. Présentation

La découverte des propriétés optoélectroniques des couches minces ferroélectriques de type perovskite a ouvert la voie à l'exploration de nouvelles approches pour la conversion de l'énergie incluant le domaine des photovoltaïques (PV). Sans l'introduction d'une jonction p-n (cas de cellules PV conventionnelles à base de semi-conducteurs), la polarisation ferroélectrique de type de couches minces induit un champ électrique interne fort exploitable pour assurer la séparation des porteurs de charges photogénérées et donc la génération d'une photo-tension (Voc). Cet effet est communément appelé l'effet photovoltaïque massif (EPM). De plus, il a été démontré que des

sauts de potentiel électrique peuvent se produire à travers certains types de parois de domaines présents dans les ferroélectriques, dont leur géométrie particulière permet la génération d'un Voc total dépassant largement le gap optique de tels matériaux.[1] Le $Pb(Zr,Ti)O_3$ (PZT), $BiFeO_3$ (BFO) and Bi_2FeCrO_6 (BFCO) constituent les matériaux les plus étudiés pour les applications PVs. L'effet photovoltaïque massif fut précédemment découvert dans de nombreux ferroélectriques permis lesquels le $LiNbO_3$,[2,3] $BaTiO_3$[4] and PZT.[5] A ce jour, les couches minces de PZT dopées au lanthanum exhibent une efficacité de conversion la plus élevée, ~ 0.005%, sous une illumination équivalente à 1 soleil.[6] Une efficacité quantique externe de l'ordre de 10% et une efficacité de conversion de 6 % sous lumière rouge ont été récemment obtenues respectivement dans le BFO[7] et le BFCO.[8] Dans ces derniers, qui sont des pérovskites à base de bismuth (Bi), leur polarisation spontanée est créé par le déplacement de ions de Bi suivant des directions spécifiques de la maille cristalline. Ceci est dû à la présence des orbitales $6s^2$ du Bi, occupant un espace important qui contraint la maille cristalline à se déformer. Ces matériaux possèdent des propriétés multiferroiques uniques, i.e. coexistence de la ferroélectricité et un ordre magnétique (ions de transition métallique avec des électrons d'orbitale d non appariés). Sous forme de couches épitaxiées [9,10] ces derniers constituent un atout pour les applications PVs puisqu'ils possèdent (i) une forte polarisation unidirectionnelle et (ii) les gaps optiques faibles (typiquement 1.4-2.7 eV) en comparaison avec les ferroélectriques conventionnels dont la valeur est autours de 3-4 eV. De plus le $BiMnO_3$ (BMO) qui exhibe un gap le plus petit, 1.2 eV, est considéré comme étant l'« atome d'hydrogène » des matériaux multiferroiques [11] et un candidat prometteur pour des applications dans le domaine PV.

Ceci dit, les efficacités de conversion de ces matériaux restent trop faibles, en deçà des valeurs théoriques et le ou les mécanismes régissant leurs propriétés PVs sont toujours méconnus. En effet, les densités de photo-courants observées sont souvent insignifiants, de l'ordre de quelques nA/cm^2, essentiellement dû à leurs larges gaps optiques et leur grande résistivité électrique. Par conséquence, ces résultats décourageants limitent sérieusement le potentiel d'intégration de ces matériaux comme couches actives dans les dispositifs PVs réels.

En vue des récentes investigations référées dans la littérature, ce constat a été totalement reconsidéré. En effet Yang et al.[1] a démonté que les parois de domaines peuvent être a l'origine

de l'effet PV dans les couches de BFO et génèrent une tension en circuit ouvert (Voc) de 15V. Une autre étude faite par M. Alexe et Hesse[12] a mise en évidence l'augmentation drastique de l'effet PV (jusqu'à 30 V) dans les cristaux de BFO quand l'air de collecte des photocharges est de l'ordre de quelques nm^2. Néanmoins, ces deux études mettent particulièrement en exergue les différents aspects et le caractère complexe des mécanismes mis en jeu pour la génération et la séparation des porteurs de charges dans ces matériaux multiferroiques. Ces dans ce context que s'inscrit mon travail de recherche dont l'objectif principal est de contribuer à la compréhension de ces phénomènes par le biais d'investigations des propriétés PV de certains systèmes multiferroiques. Il est attendu que lorsque la dimension de ce type de matériaux est réduite a l'échelle nanométrique (l'épaisseur des couches minces dans notre cas), ces derniers exhibent des propriétés fascinantes comparées à leur forme massif.

Sachant le caractère isolant des multiferroiques, le défi principal ici consiste à trouver une approche expérimentale pour améliorer l'efficacité de conversion de l'énergie solaire des couches minces de ces matériaux. Dans ce travail, l'approche consiste d'une part, à fabriquer artificiellement ces matériaux par la superposition alternative et périodique de couches minces de BFO et de BiCrO3 (BCO) sur des substrats de type perovskite LaAlO3 (LAO). Ces substrats sont enduits de couches conductrices tampon CaRuO3 pour assurer la croissance épitaxiale au moyen de l'ablation laser (PLD) de l'heterostructure BFO/BCO et réaliser les mesures électriques et PVs. Nos observations démontrent une efficacité de conversion remarquable de ces hétérostructures et mettent en évidence le rôle prépondérant de la polarisation ferroélectrique dans la génération de l'effet PV. De l'autre part, notre étude est dirigée vers l'investigation des propriétés PVs des couches minces de Bi-Mn-O déposées directement sur des substrats conducteurs de SrTiO3 dope au Niobium (STO :Nb). Le mécanisme de la polarisation ferroélectrique modulée par l'effet des interfaces Film/électrodes est mis en avance pour expliquer l'effet PV observé dans ce système.

3. Propriétés des materiaux multiferroiques

Définition

Un matériau qui exhibe plus d'un ordre ferroique (c.-à-d. ferroélectricité, ferroélasticité et magnétisme) au sein de la même phase est appelé multiferroique. Une importance toute particulière est donnée aux matériaux dans lesquels la ferroélectricité et un ordre magnétique (c.-à-d. ferri/ferromagnétique ou antiferromagnétique). Par exemple le BFO, un matériau largement étudié, possède simultanément des propriétés ferroélectrique et antiferromagnétique à température ambiante. Les matériaux multiferroiques sont classés suivant deux groupes : (i) matériaux dont les origines de la ferroélectricité et le magnétique sont indépendants et (ii) matériaux ou le magnétisme génère la ferroélectricité. Le second groupe réunit l'un des aspects les plus attrayants de matériel multiferroique et référencé comme "magnetoelectriques (ME) ". L'interdépendance des propriétés précitées dans un tel matériau est illustrée sur la Figure 1, qui étend l'application de ce type de matériaux en électronique de spin ou la spintronique.

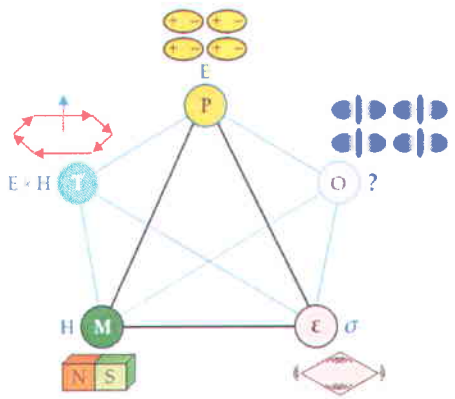

Figure 1 Représentation schématique des interactions et des couplages dans les multiferroiques. «T» représente les moments toroïdaux et «O» représente d'autres possibilités de couplage tel que celles impliquant les ordres orbitaires réversibles, les vortex et chiralités **[13].**

Du point de vue de la structure cristallographique, les matériaux multiferroïques sont divisés en quatre classes: les oxydes perovskites tels que le BFO, TbMnO3; les oxydes hexagonaux par exemple les RMnO3 où R = Ho, Er, Tm, Yb, Lu, et Y et Sc; les boracites p.ex. M3B7O13X où M est un ion métallique bivalent (M = Cr, Mn, Fe, Co, Cu, Ni) et X = Cl, Br, I, et les composés BaMF4 où M = Mg, Mn, Fe, Co, Ni, Zn.[14]

Dans ce travail, cependant, nous nous concentrons sur la structure perovskite, plus spécifiquement sur les oxydes complexes de type pérovskite, car de nombreux matériaux présentant cette structure possèdent des propriétés intéressantes du point de vue fondamental et pratique telles que : une bonne ferroélectricité, de grandes constantes diélectriques, la supraconductivité, ferromagnétisme et antiferromagnétisme. [15] La plupart de ces oxydes complexes sont abondants et contiennent deux ou plusieurs cations de métaux de transition (typiquement de type 3d) liés à l'oxygène dont la nature de leur interactions sont à l'origine de leurs propriétés uniques.

La formule chimique générale de la structure perovskite est ABX3 ou A2BB'X6 (pour la double perovskite) où «A» désigne un cation non magnétique et 'B' désigne un cation magnétique. La **Figure 2** illustre la maille unitaire de la pérovskite de type ferrite de bismuth, BFO. La pérovskite BFO est de type rhomboherale et présente une excellente polarisation spontanée (~ 100 $\mu C/cm^2$ à température ambiante) [16, 17] avec une température de transition ferroélectrique élevée (T_C = 1103 K) et un antiferromagnétisme (très faible ferromagnétisme) au-dessous de la température de Néel (T_N = 643K).

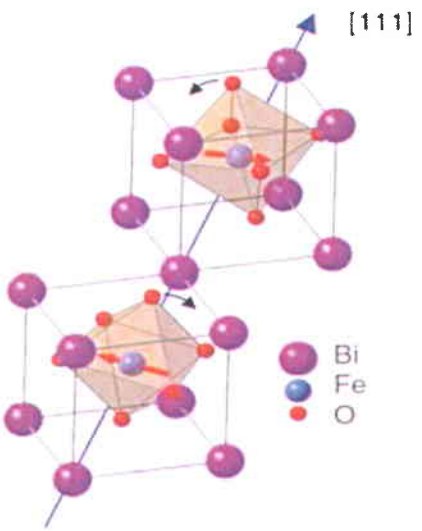

Figure 2 Schéma de la structure typique du composé $BiFeO_3$ [18]

Dans les matériaux ferroélectriques classiques, la ferroélectricité provient du cation non magnétique et non centrosymétrique qui se déplace à certaine une distance par rapport centre de

gravité des anions environnants. Ce décalage entre les charges positives et négatives donne lieu à un moment dipolaire électrique. En revanche, dans un matériau magnétique, le cation magnétique (ayant une orbitale d partiellement occupée) a tendance à se positionner exactement au centre des anions environnants (la position centrosymétrique est ainsi favorisée), ce qui entraîne l'absence d'un moment dipolaire. La coexistence de la ferroélectricité et du magnétisme au sein de la même phase d'un matériau multiferroique signifie l'existence d'une compétition entre les énergies d'hybridation et de répulsion coulombienne aux niveaux des liaisons covalentes. [19] L'équilibre entre les deux énergies favorise une décentralisation de l'un cation du site A, Bi3 + dans le cas du BFO, pour aboutir à l'apparition d'un moment dipolaire et un comportement ferroélectrique. En d'autres termes, ferroélectricité peut ainsi générée de l'instabilité structurelle qui est compatible avec la coexistence du magnétisme.[20, 21, 22]

Matériaux multiferroiques pour des applications dans le photovoltaïque

Dans les dispositifs PVs conventionnels basés sur des jonctions n-p, les porteurs de charge photogénérés sont entraînés par le champ électrique [23] créé dans la région de déplétion. Cela signifie que la tension en circuit ouvert (Voc) est dans ce cas limitée par la bande interdite (Eg) du matériau, normalement inférieure à la largeur de bande (eV_{OC} <Eg). En revanche, dans le cas de l'effet PV dans les ferroélectriques, les électrons et des trous photogénérés sont en outre séparés par le champ électrique interne présent dans ces matériaux, induit par la polarisation spontanée.[24] La différence fondamentale entre ces deux types de dispositifs PV réside dans l'ampleur et la portée de leurs forces motrices des porteurs de charges c-a-d le champ électrique. Le Champ électrique dépendant de la polarisation (champ de dépolarisation, E_{DP}) dans le matériau ferroélectrique est d'au moins un ordre de grandeur plus élevé que dans les dispositifs à base de jonction np classiques.

De plus, ce champ de dépolarisation n'est pas confiné dans une petite zone comme c'est le cas de l'interface p-n. Semblable à la jonction n-p, les MFs à faibles bandes interdites possèdent un comportement ferroélectrique qui développe un champ électrique dans tout le volume du matériau, un paramètre clé pour la séparation efficace des charges photogénérées dans les dispositifs photovoltaïques. Le mécanisme de l'effet photovoltaïque dans les MFs peut être expliqué de façon similaire que le mécanisme a l'origine de celui impliquant une jonction p-n, comme illustré à la **Figure 3**. Ici, dans le cas des films minces de BFO ayant une distribution de

parois de domaines ferroélectriques particulière, des changements brusques de la polarisation peuvent survenir aux frontières de ces domaines. Ce déséquilibre de charges crée une chute de potentiel électrostatique (typiquement entre 0,02 à 0,2 eV) à travers la paroi de domaine qui est responsable du fléchissement des bandes de valence (BV) et de conduction (BC) au niveau cette région.[25] Notez que la paroi de domaine est beaucoup plus mince (2 nm) que la zone de déplétion d'une jonction n-p. Par conséquent, la séparation de charge est beaucoup plus efficace et plus rapide au niveau de ces parois de domaines.

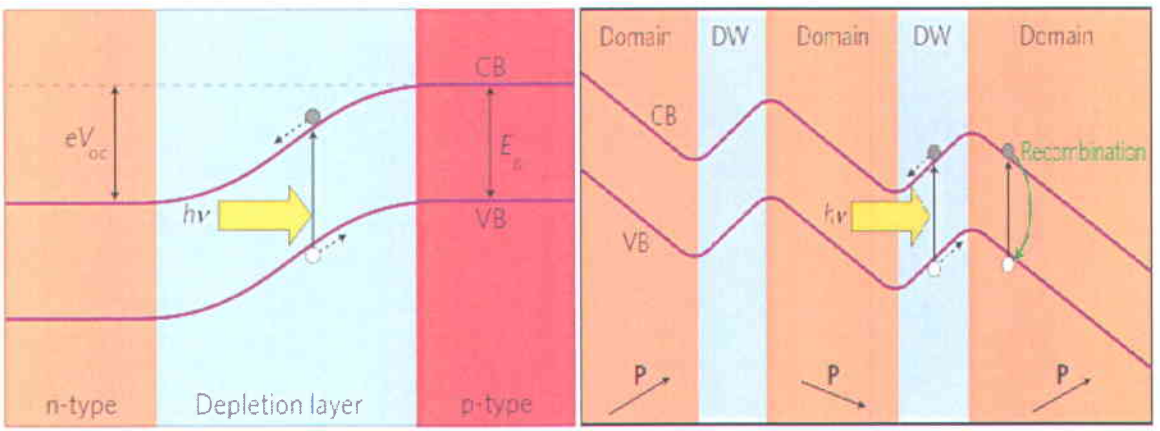

Figure 3 Schéma représentant le diagramme des bandes dans une jonction p-n et le fléchissement des bandes dans les multiferroiques. Figure adaptée à partir de la référence [25].

Pour les cellules solaires à base de couches minces de MFs, des électrodes sont également en contact direct avec les films qui crée en général des contacts de type Schottky à l'interface film/ électrode. Par conséquent, le champ électrique interne responsable du déplacement des porteurs de charge est une combinaison de deux éléments: (i) le champ de dépolarisation (E_{DP}) provenant de l'orientation de la polarisation dans la majeure partie du film, et (ii) champ électrique de l'interface (Ei) résultant des interfaces électrode-couche. Comme illustré sur la **Figure 4**, le champ de dépolarisation (E_{DP}) originaire de la polarisation spontanée et opposée à la direction de cette dernière, et le champ électrique de l'interface (Ei) est indépendant de la polarisation, et il provient des contacts de type Schottky produits aux interfaces électrode-couche.

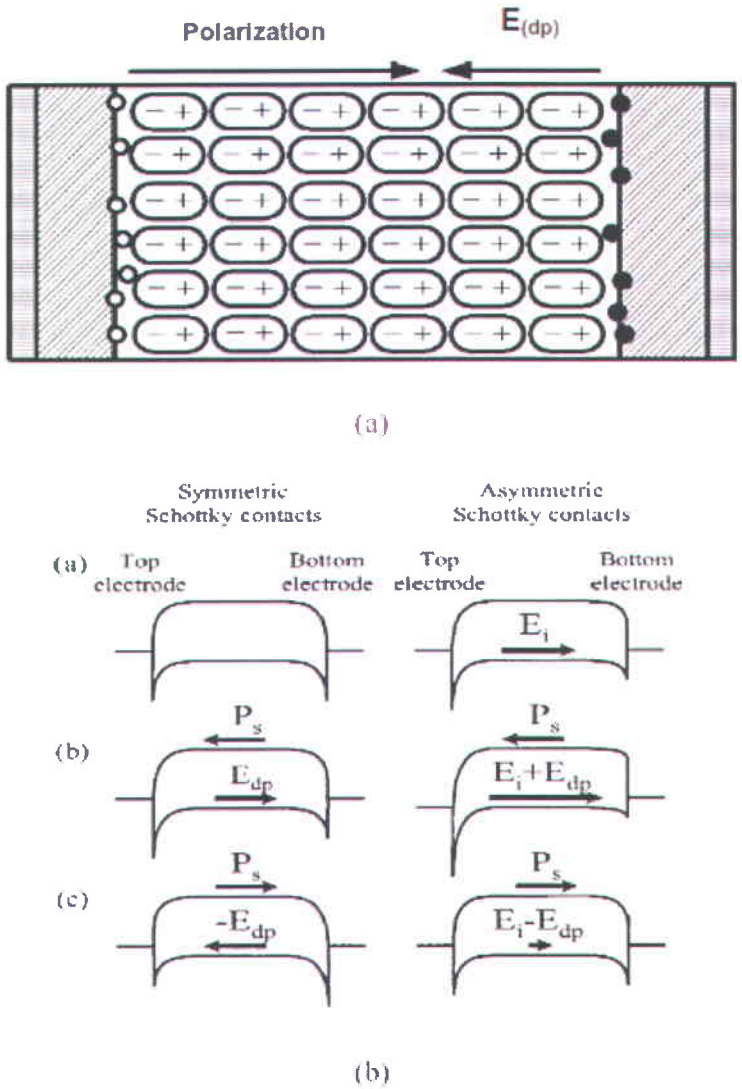

Figure 4 (a) L'effet de l'interface sur la tension Voc dans un matériau ferroélectrique possédant un champ dépolarisation (E_{DP}).[26] (b) Schémas représentants les contacts Schottky symétriques et asymétriques indiquant le champ électrique Ei crée aux interface métal-film-métal.[27]

Toutefois, l'efficacité de conversion de puissance des dispositifs basés sur les MFs est encore faible en raison de la faible conductivité volumique des MFs, comparée à celle d'une cellule solaire à base de silicium disponible dans le commerce. Ceci est expliqué comme suit: pour que la ferroélectricité existe dans un matériau MF, celui-ci doit être naturellement isolant, sinon les charges mobiles vont écranter la polarisation électrique et diminuer sa portée. [28] En fait, tous les efforts pour augmenter la conductivité des matériaux MFs se traduisent par une

réduction de la polarisation spontanée, et par conséquence, celle du champ électrique interne. Etant donné que ce dernier est directement lié à la séparation des porteurs de charges photogénérées, il en résulte une efficacité de conversion d'énergie plus faible. Cependant, une nanostructuration efficace et optimale de ces matériaux pourrait être un moyen efficace pour améliorer l'efficacité PV.

Structure de la thèse

Le chapitre 2 décrit brièvement les méthodes expérimentales utilisées tout au long de ce travail de recherche. Il y a tout d'abord, la technique de dépôt par laser pulsé (PLD), un outil le plus adapté pour la croissance de films minces d'oxydes complexes, ou l'effet de plusieurs paramètres clés influant la qualité des films minces, tels que, la pression partielle et la température de croissance est discutée. Ensuite, le chapitre aborde les différentes techniques de caractérisation des couches minces utilisées pour analyser les échantillons élaborés durant ma recherche. Par exemple, la diffraction des rayons X (DRX)) est utilisée pour analyser la structure cristalline et la phase des couches minces produites. Les microscopies à force atomique (AFM) et électronique à balayage (MEB) ont été employées pour visualiser la topographie de surface. L'étude des propriétés ferroélectriques des couches à l'échelle nanométrique a été réalisée au moyen de la microscopie a force piézoélectrique (PFM). L'absorption optique et la bande interdite ont été mesurées par ellipsométrie.

Enfin, des expériences employant un simulateur solaire ont été menées pour déterminer les valeurs du photocourant et la phototension des dispositifs à base des matériaux étudiés, qui sont à la base de calcul de l'efficacité de conversion. Le chapitre 3 présente les résultats expérimentaux de l'efficacité PV obtenues pour les hétérostructures de $BiFeO_3/BiCrO_3$ déposées sur des substrats de $LaAlO_3$. Cette étude a mis en exergue la dépendance de la phototension et du photocourant au nombre de bicouche BFO/BCO incorporée dans la structure. En raison des bandes interdites similaires de BFO et BCO, la dépendance en épaisseur de la profondeur d'absorption (suivant la loi de Beer-Lambert) a été employée pour expliquer la nature des tensions et des courants photoélectriques observés. Dans le chapitre 4, nous présentons l'effet PV des couches minces de Bi-Mn-O, des résultats jamais reportés auparavant. Nous présentons une étude comparative de l'efficacité PV de trois couches minces de Bi-Mn-O ayant des rapports Bi :Mn différents et dont la croissance est réalisée sur des substrats de STO :Nb orientés (111).

Un rapport Bi / Mn élevé dans la couche démontré une efficacité de conversion la plus significative. Les phénomènes PV observés sont expliqués par l'effet combiné de la polarisation ferroélectrique et des interfaces film / électrodes. Le chapitre 5 décrit la conclusion générale de mon travail de recherche et discute quelques perspectives à suivre pour compléter certains aspects de cette recherche.

4. Références

[1] S. Y. Yang, J. Seidel, S. J .Byrnes, P. Shafer, C.-H. Yang, M . D .Rossell, J. F. Scott, J. W. Ager, L.W. Martin, P. Yu, Y.-H. Chu, and R. Ramesh, Nature Nanotech. **5**, 143 (2010)

[2] A. M. Glass, D. von der Linde, and T. J. Negran, Appl. Phys. Lett. 25, 233 (1974)

[3] A. M. Glass, D. Von der Linde, D. H. Auston, and T. J. Negran, J. Electron. Matter. 4, 915 (1975)

[4] V. M. Fridkin and B. N. Popov, Sov. Phys. Usp. 21, 981 (1978)

[5] P. S. Brody and F. Crowne, J. Electron. Matter. 4, 955 (1975)

[6] M. Qin, K. Yao, and Y. C. Liang. Appl. Phys. Lett. 93, 122904 (2008)

[7] S. Y. Yang, L. W. Martin,S. J. Byrnes,T. E. Conry,S. R. Basu,D. Paran, L. Reichertz, J. Ihlefeld, C. Adamo,A. Melville,Y.-H. Chu, C.-H. Yang, J. L. Musfeldt,D. G. Schlom, J. W. Ager and R. Ramesh, Appl. Phys. Lett. 95, 062909 (2009).

[8] R. Nechache, C. Harnagea, S. Licoccia, E. Traversa, A. Ruediger, A. Pignolet, and F. Rosei Appl. Phys. Lett. 98, 202902 (2011).

[9] J. Wang et al. Science 299, 1719-1722 (2003)

[10] R. Nechache, C. Harnagea, A. Pignolet, F. Normandin, T. Veres, L. -P. Carignan, and D. Ménard, Appl. Phys. Lett. 89, 102902 (2006)

[11] N. A. Hill and K. M. Rabe, Phys. Rev. B 59, 8759 (1999).

[12] M. Alexe, Nano Letters **12**, 2193-2198 (2012).

[13] N. A. Spaldin, S. W. Cheong, and R. Ramesh, Physics Today, P-38, October 2010

[14] G. A. Smolenskii, I. E. Chupis, Ferroelectric magnetic materials, Usp. Fiz. Nauk 137, 415-448 (1982) (in Russian)

[15] Y. Tokura, Colossal Magnetorestive Oxides, Gordon and Breach Science Publishers, Amsterdam, Netherlands, 2000

[16] J. Wang, J. B. Neaton, H. Zheng, V. Nagarajan, S. B. Ogale, B. Liu, D. Viehland, V. Vaithyanathan, D. G. Schlom, U. V. Waghmare, N. A. Spaldin, K. M. Rabe, M. Wuttig, R. Ramesh, 299, 1719-1722, Science 2003

[17] K. Yun, D, Ricinschi, T. Kanashima, M. Noda, M. Okuyama, Jpn. J. Appl. Phys. **2004**, 43, L647-L648

[18] http://cdn.intechopen.com/pdfs/44929/InTech-Optical_properties_of_multiferroic_bifeo3_films.pdf

[19] Lines and Glass, Ferroelectrics and related materials, Oxford (1977)

[20] B. B. van Aken, T. T. M. Palstra, A. Filippetti, & N. A. Spaldin, Nature Mater. **3,** 164–170 (2004)

[21] C. J Fennie, K. M. Rabe, Phys. Rev. B **72,** 100103(R) (2005)

[22] C. Ederer, N. A. Spaldin, Phys. Rev. B **74,** 1 (2006)

[23] S. M. Sze, Physics of Semiconductor Devices, 2nd edn (John Willey & Sons), 1981

[24] Meng Quin, Kui Yao, Yung C. liang, Appl. Phys. Lett. 93, 122904, 2008

[25] Haitao Huang, Nature photonics, vol 4, March 2010

[26] Q. Meng, Y. Kui, and C. L. Yung, Applied Physics Letters, 93 (12), p.122904 (2008)

[27] Y. S. Yang, S. J. Lee, S. Yi, B. G. Chae, S. H. Lee, H. J. Joo, M. S. Jang, Applied Physics Letters, 76 (6), p. 774-776. (2000)

[28] R. Ramesh, N. Spaldin, Nature Materials, Vol. 6, January (2007)